

Imaging inter-valley coherent order in magic-angle twisted trilayer graphene

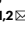
<https://doi.org/10.1038/s41586-023-06663-8>

Received: 5 May 2023

Accepted: 21 September 2023

Published online: 15 November 2023

 Check for updates

Hyunjin Kim^{1,2,3,10}, Youngjoon Choi^{4,10}, Étienne Lantagne-Hurtubise^{2,3}, Cyprian Lewandowski^{2,3,5,6}, Alex Thomson^{2,3,7,8}, Lingyuan Kong^{1,2}, Haoxin Zhou^{1,2}, Eli Baum^{1,2}, Yiran Zhang^{1,2,3}, Ludwig Holleis⁴, Kenji Watanabe⁹, Takashi Taniguchi⁹, Andrea F. Young⁹, Jason Alicea^{2,3,7} & Stevan Nadj-Perge^{1,2}

Magic-angle twisted trilayer graphene (MATTG) exhibits a range of strongly correlated electronic phases that spontaneously break its underlying symmetries^{1,2}. Here we investigate the correlated phases of MATTG using scanning tunnelling microscopy and identify marked signatures of interaction-driven spatial symmetry breaking. In low-strain samples, over a filling range of about two to three electrons or holes per moiré unit cell, we observe atomic-scale reconstruction of the graphene lattice that accompanies a correlated gap in the tunnelling spectrum. This short-scale restructuring appears as a Kekulé supercell—implying spontaneous inter-valley coherence between electrons—and persists in a wide range of magnetic fields and temperatures that coincide with the development of the gap. Large-scale maps covering several moiré unit cells further reveal a slow evolution of the Kekulé pattern, indicating that atomic-scale reconstruction coexists with translation symmetry breaking at a much longer moiré scale. We use auto-correlation and Fourier analyses to extract the intrinsic periodicity of these phases and find that they are consistent with the theoretically proposed incommensurate Kekulé spiral order^{3,4}. Moreover, we find that the wavelength characterizing moiré-scale modulations monotonically decreases with hole doping away from half-filling of the bands and depends weakly on the magnetic field. Our results provide essential insights into the nature of the correlated phases of MATTG in the presence of strain and indicate that superconductivity can emerge from an inter-valley coherent parent state.

Spontaneous symmetry breaking lies at the foundation of condensed matter physics, as the emergence of previously unknown quantum phases often accompanies symmetry reduction. Superconductivity and magnetism provide canonical examples that emerge when charge conservation and spin-rotation symmetry, respectively, are broken. In the strongly correlated realm, superconductivity commonly occurs in conjunction with other forms of symmetry breaking^{5,6}, and investigating their intricate relation presents a profound challenge relevant for many platforms—including the growing family of twisted graphene multilayers^{1,2,7,8}. Scanning tunnelling microscopy (STM) is a well-established tool for identifying certain symmetry-broken states, particularly those that leave direct signatures in real space through the local density of states (LDOS) distribution. Nevertheless, the inherently difficult task of creating large, sufficiently clean and low-strained areas in magic-angle twisted multilayers has so far prevented the STM from generating spatial maps of electronic structures sufficient for unambiguously diagnosing microscopic symmetry-breaking order. Previous studies have, therefore, focused mostly on observing spectroscopic signatures combined with basic structural characterization^{9–12},

especially in the context of magic-angle twisted trilayer graphene (MATTG)^{13,14}. Only very recently, this challenge has been resolved in twisted bilayers¹⁵, but, to our knowledge, MATTG has not been explored in the context of symmetry-breaking orders.

Imaging Kekulé distortion in MATTG

Figure 1a shows the STM measurement setup and the structure of twisted trilayer graphene (TTG), in which the second layer is twisted by an angle θ , and the first and third layers are aligned. This configuration is known to exhibit an electronic structure that, in the absence of a perpendicular electric field, hosts flat bands similar to that of twisted bilayer graphene and an additional set of dispersive Dirac cones^{16,17}. We focus on an area with low heterostrain ($\epsilon \approx 0.12\%$) and a twist angle $\theta = 1.60^\circ$, close to the magic-angle value of TTG (see Methods and Extended Data Figs. 1 and 2 for fabrication details). High-resolution imaging that resolves the atomic scale of TTG near an AAA site—for which carbon atoms on all three layers are aligned (Fig. 1b,c)—shows a honeycomb structure with a lattice constant of 0.246 nm accompanied

¹Thomas J. Watson, Sr, Laboratories of Applied Physics, California Institute of Technology, Pasadena, CA, USA. ²Department of Physics, California Institute of Technology, Pasadena, CA, USA.

³Institute for Quantum Information and Matter, California Institute of Technology, Pasadena, CA, USA. ⁴Department of Physics, University of California, Santa Barbara, Santa Barbara, CA, USA.

⁵National High Magnetic Field Laboratory, Tallahassee, FL, USA. ⁶Department of Physics, Florida State University, Tallahassee, FL, USA. ⁷Walter Burke Institute for Theoretical Physics, California

Institute of Technology, Pasadena, CA, USA. ⁸Department of Physics, University of California, Davis, Davis, CA, USA. ⁹National Institute for Materials Science, Tsukuba, Ibaraki, Japan. ¹⁰These

authors contributed equally: Hyunjin Kim, Youngjoon Choi. ✉e-mail: hyunjin@caltech.edu; s.nadj-perge@caltech.edu

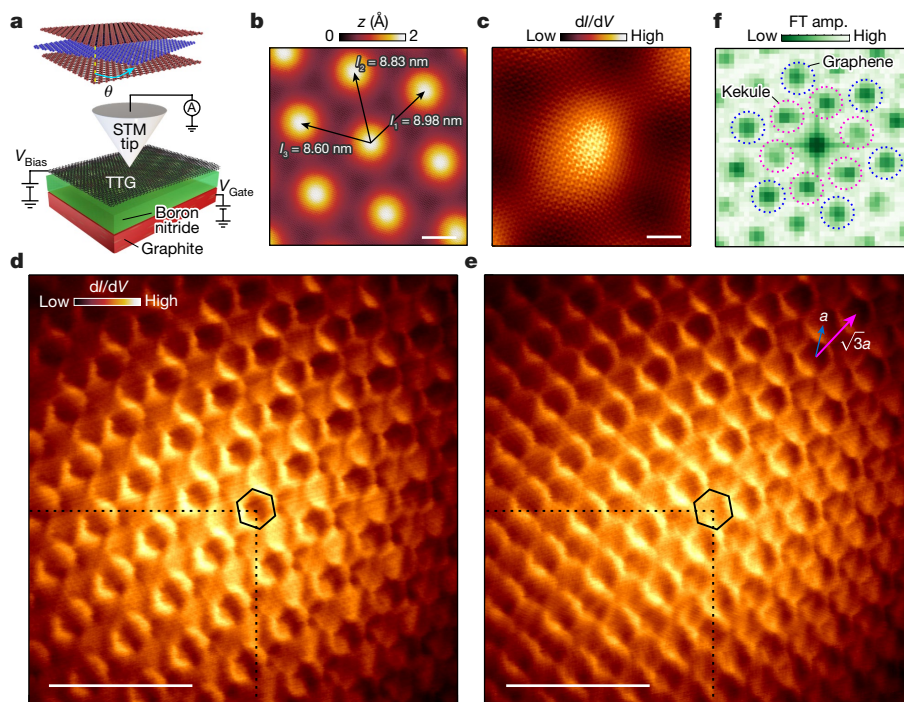


Fig. 1 | Overview of the experiment and atomically resolved maps revealing Kekulé pattern. **a**, Schematic depicting TTG (top) and device geometry used for the STM measurements (bottom). **b**, Atomically resolved topography showing the moiré lattice used to extract the magnitude of heterostrain $|e| \approx 0.12\%$ and twist angle $\theta = 1.60^\circ$. **c**, Tunneling conductance map taken at $V_{\text{Gate}} = -9$ V and $V_{\text{Bias}} = -2$ mV at the AAA site showing atomic resolution. **d, e**, dI/dV map measured at fixed $V_{\text{Gate}} = -10.3$ V and negative $V_{\text{Bias}} = -2$ mV (**d**)

and positive $V_{\text{Bias}} = 2$ mV (**e**) with further magnification into the AAA site and showing contrast inversion on change of V_{Bias} . **f**, Fourier transformation of **d** showing well-resolved peaks corresponding to graphene lattice and Kekulé reconstruction. Data in **d** and **e** were taken at $T = 400$ mK. Unless otherwise specified, data are taken at $T = 2$ K. amp., amplitude. Scale bars, 4 nm (**b**); 2 nm (**c**); and 1 nm (**d, e**).

by a more subtle larger-scale atomic modulation. This modulation, although visible in topography, is more prominent in the dI/dV spatial maps (Fig. 1d,e) that show a clear lattice-tripling pattern, the intensity of which depends sensitively on the applied bias voltage V_{Bias} , with the contrast approximately inverting on changing the sign of V_{Bias} (Extended Data Fig. 3). Fourier analysis of the dI/dV maps further confirms the periodicity of this pattern (Fig. 1f): a set of six outer peaks corresponding to the graphene lattice is accompanied by six inner peaks that correspond to $1/\sqrt{3}$ of the graphene reciprocal lattice vectors rotated by 30° . This enlargement of the graphene unit cell into a $\sqrt{3} \times \sqrt{3}$ supercell rotated by 30° corresponds to a so-called Kekulé distortion previously observed in monolayer graphene decorated with metallic adatoms¹⁸ or in the quantum Hall regime^{19,20}. In general, the observation of Kekulé distortion implies a reduction of the Brillouin zone arising from coherent scattering of electrons between the K and K' valleys, commonly referred to as the inter-valley coherence.

The observed Kekulé distortion strongly depends on gate voltage—that is, filling (Fig. 2). Focusing still on the vicinity of the AAA sites, when the MATTG Fermi level is in the remote bands (Fig. 2a,e) or near charge neutrality (Fig. 2c,g), the Kekulé distortion is completely absent. By contrast, a very prominent distortion arises at filling factors of around $-3 < \nu < -2$ (Fig. 2b,f) and $2 < \nu < 3$ (Fig. 2d,h). Figure 2i summarizes the observed relative Kekulé peak intensity compared with the graphene lattice peaks. The regions of non-zero intensity match well with the regions that host either an insulating gap or pseudogap in the gate spectroscopy (Fig. 2j; see also Extended Data Fig. 9 for data on another sample). The relative intensity of the Kekulé peaks depends strongly on the bias voltage and is approximately maximized when V_{Bias} matches the LDOS peak accompanying the (pseudo) gap (Extended Data Fig. 4). Moreover, at higher temperatures, as the gap is suppressed, the visibility of Kekulé peaks also diminishes (Extended Data Fig. 4).

Strong dependence of the reconstruction on V_{Gate} , V_{Bias} and the temperature indicates its electronic origin and rules out the possibility that the observed Kekulé peaks arise from impurities or structural deformations.

Various inter-valley coherent (IVC) phases have been theoretically proposed as the ground state of magic-angle twisted bilayers^{3,21–23}, with a limited number of theoretical calculations specific to MATTG²⁴. We consider the family of these candidate IVC phases, motivated by refs. 25,26 and the close band structure and spectroscopic resemblances between twisted bilayers and trilayers. One member of this family—the Kramers IVC phase—was predicted to appear in unstrained samples^{21–23} and manifests as a magnetization density wave that generates Kekulé peaks in the LDOS at only finite magnetic fields^{25,26}. As we observe pronounced Kekulé peaks already at zero magnetic field, this IVC order can be ruled out in our MATTG samples. Two other leading candidates include the time-reversal-symmetric IVC and incommensurate Kekulé spiral (IKS) phases; both produce charge density waves that generate LDOS Kekulé peaks at zero magnetic field, compatible with our measurements.

Moiré translation symmetry breaking

To establish the nature of the correlated state more precisely, we investigate the variations of the Kekulé pattern across the neighbouring moiré unit cells by taking large-area dI/dV maps (at $\nu = -2.3$) covering a region of 36 nm \times 36 nm that encompasses 20 moiré AAA sites (Fig. 3a). Focusing first on two regions around neighbouring AAA sites (Fig. 3b,e; marked by a yellow and blue square in Fig. 3a), we decompose the map by Fourier transform filtering to separate the spatial evolution of the Kekulé distortions from the underlying graphene lattice (Methods). These regions are chosen to have graphene lattices that are atomically

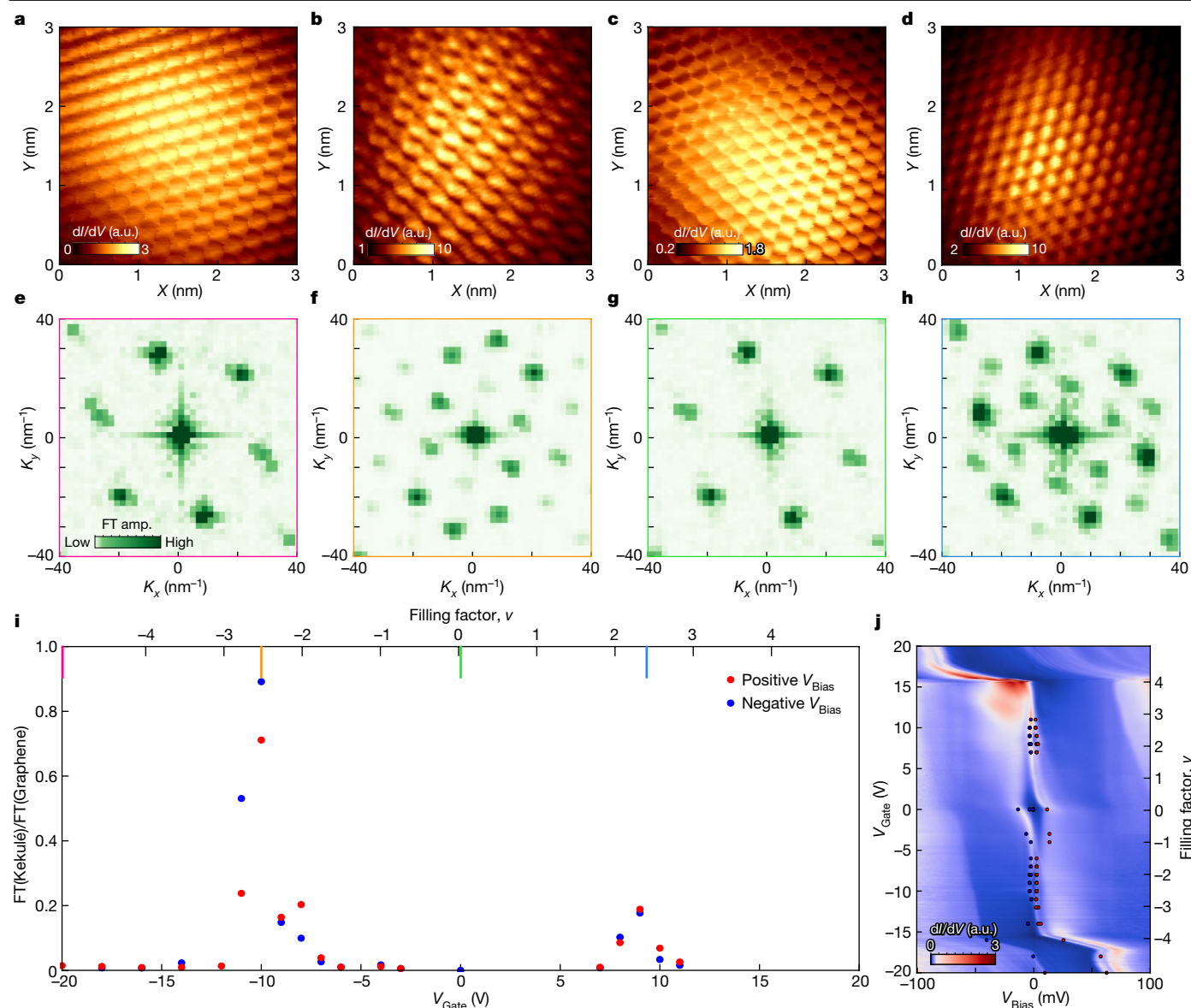


Fig. 2 | V_{Gate} -dependent mapping of Kekulé order on MATG. **a–d**, Real-space dI/dV map at $V_{\text{Gate}} = -20$ V (**a**), -10 V (**b**), 0 V (**c**) and 9 V (**d**), taken at $V_{\text{Bias}} = 63$ mV (**a**), -3 mV (**b**), -13 mV (**c**) and 3 mV (**d**), tracking the evolution of the flat-band density of states. **e–h**, Fourier transform (FT) of **a–d** magnified to show the peaks corresponding to graphene and Kekulé reciprocal lattice vectors. In addition to graphene and Kekulé peaks, in **f** and **h** higher-order peaks are also resolved. **i**, Intensity of the peaks at Kekulé reciprocal lattice vector normalized by the

intensity of the peaks at graphene reciprocal lattice vector as a function of V_{Gate} . The intensities at all six Kekulé peaks are summed up and divided by the sum of six graphene peak intensities. Blue and red dots correspond to averaged data across positive (negative) V_{Bias} values for each V_{Gate} (all the values are marked in **j**). **j**, V_{Gate} -dependent dI/dV spectroscopy measured on the same area for which **a–h** is measured. a.u., arbitrary unit.

aligned precisely (Fig. 3c,f). Under these conditions, although the raw data show only subtle differences, Fourier-transform-filtered Kekulé patterns show that bright spots (high intensity) in the yellow window (Fig. 3d) become dark spots (low intensity) in the blue window (Fig. 3g) and vice versa. This dichotomy establishes that the Kekulé distortion between two neighbouring moiré sites changes markedly. We note that, in general, the intensity of the Kekulé distortion Fourier transform peaks and graphene reciprocal lattice peaks evolve independently across the sample.

To quantify the spatial variation across the entire mapped region, we extend the above method and create Kekulé auto-correlation maps (Fig. 3h). Here we fix a small region of approximately $1\text{ nm} \times 1\text{ nm}$ and separately auto-correlate graphene lattice- and Kekulé-filtered periodicities with a moving window of the same size that samples different map regions. The auto-correlation is normalized such that perfectly

correlated regions correspond to 1, whereas perfectly anti-correlated regions correspond to -1 . We assign Kekulé auto-correlation values to the nearest points at which atomic auto-correlation exceeds a threshold value of 0.5 (the conclusions do not depend on the exact threshold value). This procedure ensures alignment of the underlying graphene lattices when comparing Kekulé modulation across different parts of the map. The magnified map in Fig. 3h shows a rapid evolution of the auto-correlation and the atomic-scale lattice tripling (three unit cells) pattern (Fig. 3i–l; see Methods for further discussion). On the moiré length scale, this Kekulé map shows clear stripe-like red-blue patterns along the l_1 and l_2 directions but shows weak dependence along the l_3 direction. The observed periodicity reflects modulation at a wavevector $\mathbf{q}_{\text{Kekulé}}$ that is perpendicular to the l_3 direction with a magnitude that is approximately half of a moiré reciprocal lattice vector (for this filling factor)—corresponding to a near doubling of the moiré unit cell.

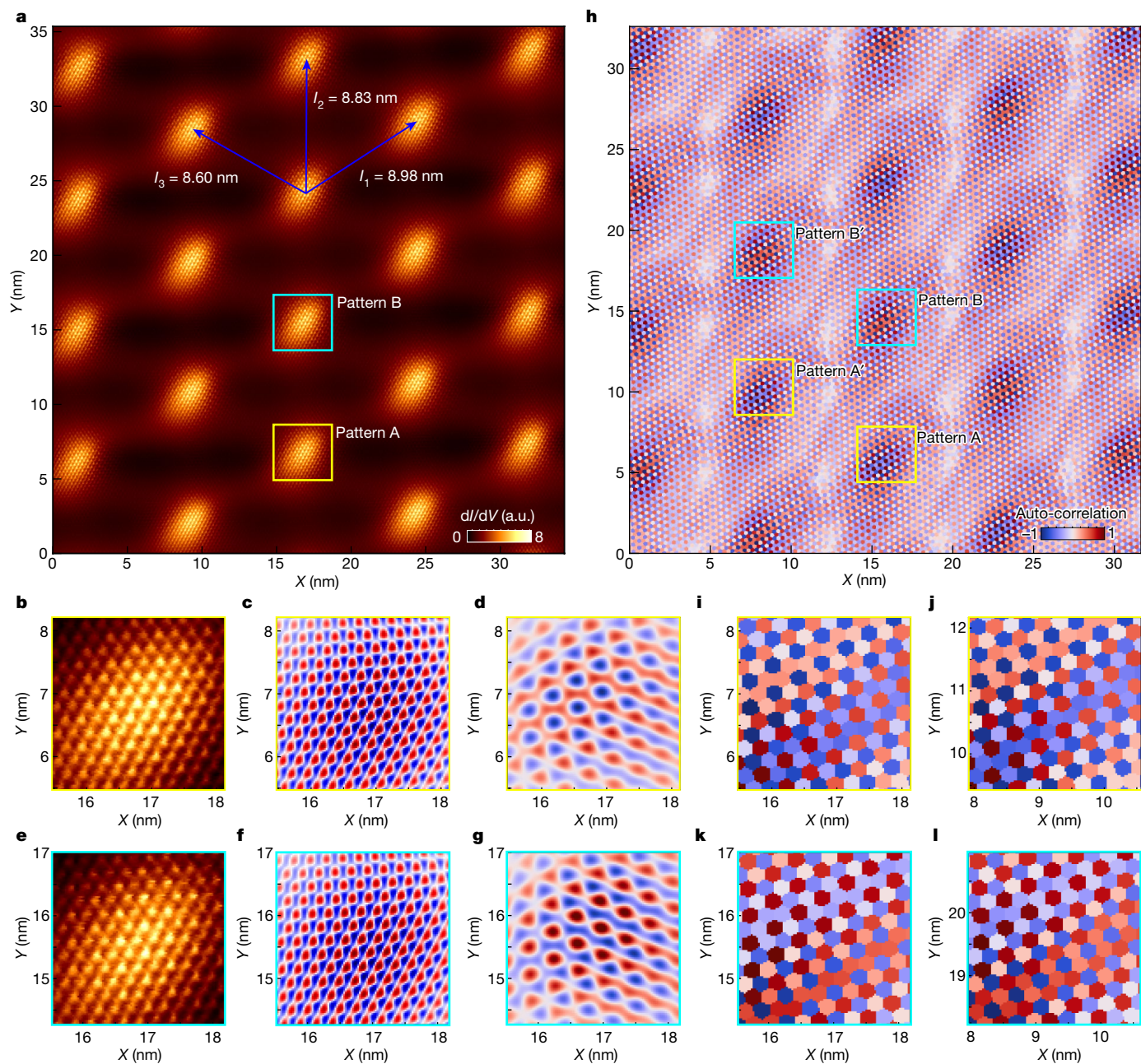


Fig. 3 | Evidence of moiré translation symmetry breaking. **a**, Large-scale area dI/dV scan around $v = -2.3$. **b, e**, A $2.2 \text{ nm} \times 2.2 \text{ nm}$ window from **a** centred on one AAA site (**b**) and its nearest-neighbour AAA site along the l_2 direction (**e**). **c, f**, Corresponding graphene Fourier-transform-filtered dI/dV map for **b, e** shows the precise alignment of the atomically resolved signals. **d, g**, Kekulé Fourier-transform-filtered dI/dV map for **b, e** showing inverted contrast between the neighbouring AAA sites. Fourier transform filtering of graphene (Kekulé) signals is performed by masking the Fourier transform image with round masks of radius 3.5 nm^{-1} around six graphene (Kekulé) Fourier transform peaks and

performing an inverse Fourier transform. **h**, Kekulé dI/dV auto-correlation map of **a**. Auto-correlation is calculated between two small windows from **a** in which one window is fixed at some position and the other spans the image (see also Methods). **i, j**, A $2.2 \text{ nm} \times 2.2 \text{ nm}$ window taken from the Kekulé auto-correlation map centred on the AAA site showing pattern A (**i**) and the neighbouring AAA site along the l_3 direction showing an almost similar pattern (**j**). **k, l**, A $2.2 \text{ nm} \times 2.2 \text{ nm}$ window taken from Kekulé auto-correlation map centred on AAA site showing pattern B (**k**) and neighbouring AAA site along the l_3 direction showing an almost similar pattern (**l**). a.u., arbitrary unit.

Kekulé modulation wavevector

Although the auto-correlation analysis shown above demonstrates that the translation symmetry on the moiré length scales is broken, obtaining the modulation periodicity directly from real-space maps is challenging when the order is far from commensurate. We, therefore, turn to a Fourier-space analysis to extract the modulation wavevectors arising over a broad filling range. Figure 4a shows the Fourier transform of the map shown in Fig. 3a. In contrast to the Fourier transform

images of the small real-space areas, here the graphene reciprocal lattice and Kekulé peaks are decorated by satellite peaks—reflecting the longer-wavelength moiré pattern in the original image. Identifying the exact graphene lattice vector peak among the cluster of satellite peaks is non-trivial, as even small errors in the STM calibration or possible homostrain effects in the top graphene layer can alter it. We overcome this problem by examining the higher-order reciprocal lattice vectors, which exhibit smaller clusters in Fourier space and thus allow for more precise extraction (Extended Data Fig. 6). In Fig. 4b–d, we mark the

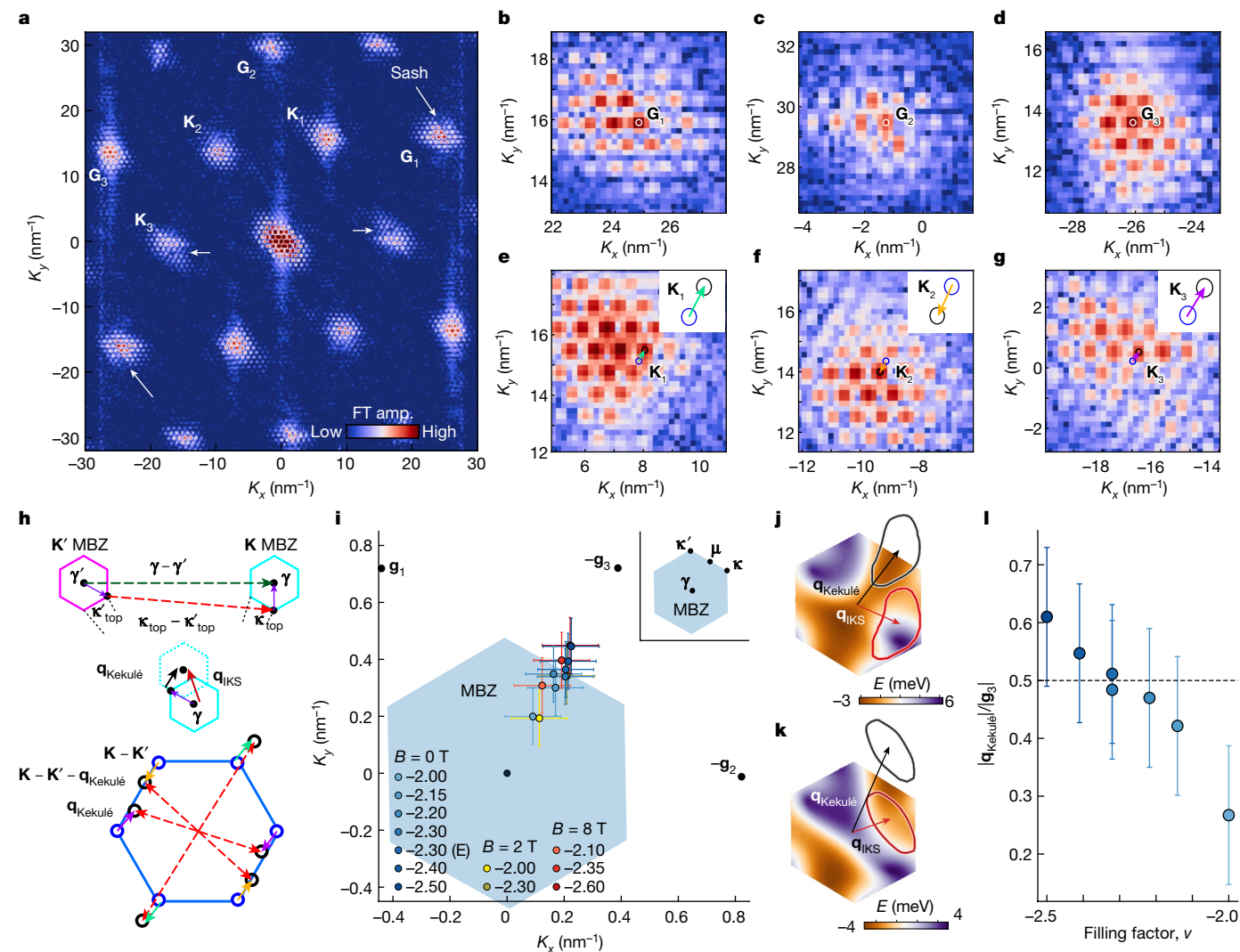


Fig. 4 | IKS wavevector extracted from the Fourier transformation maps.
a, Fourier transformation of the real space dI/dV map at $\nu = -2.3$ and $V_{\text{Bias}} = -2$ mV. Fourier transform (FT) peaks at the graphene reciprocal lattice vector site decorated with moiré satellite peaks are named \mathbf{G}_1 , \mathbf{G}_2 and \mathbf{G}_3 , whereas the peaks around the Kekulé reciprocal lattice vector position are named \mathbf{K}_1 , \mathbf{K}_2 and \mathbf{K}_3 . **b–d**, Magnified images of **a** in which the exact graphene reciprocal lattice vector positions are marked as black dots. **e–g**, Magnified images of **a** around \mathbf{K}_1 , \mathbf{K}_2 and \mathbf{K}_3 , in which the expected Kekulé reciprocal lattice vector positions are marked as blue circles. The nearest satellite peaks that are used to extract the modulation wavevector $\mathbf{q}_{\text{Kekulé}}$ are marked as black circles. Arrows denote the direction of $\mathbf{q}_{\text{Kekulé}}$ for each \mathbf{K}_1 , \mathbf{K}_2 and \mathbf{K}_3 . **h**, Schematics depicting the hybridization of \mathbf{K} and \mathbf{K}' MBZ for two different cases (top). $\boldsymbol{\gamma}$ to $\boldsymbol{\gamma}'$ (green vector) gives a Kekulé pattern that is commensurate with the moiré lattice, whereas \mathbf{k}_{top} to \mathbf{k}'_{top} (red vector) gives a spatially uniform Kekulé pattern on the graphene scale. The middle panel shows the relation between \mathbf{q}_{IKS} and $\mathbf{q}_{\text{Kekulé}}$. The bottom panel shows schematics of Fourier transform peaks corresponding

to the IVC state with finite Kekulé modulation $\mathbf{q}_{\text{Kekulé}}$. **i**, Extracted modulation wavevector $\mathbf{q}_{\text{Kekulé}}$ as a function of both V_{Gate} and out-of-plane magnetic field of 2 T and 8 T. Black dots denote the positions of moiré reciprocal lattice vectors \mathbf{g}_1 , \mathbf{g}_2 , and \mathbf{g}_3 , which are perpendicular to l_1 , l_2 and l_3 , respectively, in Fig. 1b. The blue hexagon is the MBZ calculated with the \mathbf{g}_1 , \mathbf{g}_2 , and \mathbf{g}_3 extracted from the experiment. **j, k**, Calculated band structure of the top-most valence band in the \mathbf{K} valley at filling $\nu = -2$, in the regime of small Hartree correction ($\epsilon_r = 30$) (**j**), in which the flat band is non-inverted, and in the regime of large Hartree correction ($\epsilon_r = 15$) (**k**), in which the flat band is inverted around the $\boldsymbol{\gamma}$ point of the MBZ. The black and red arrows, respectively, indicate the theoretically optimal $\mathbf{q}_{\text{Kekulé}}$ and \mathbf{q}_{IKS} wavevectors, with contours showing the corresponding confidence interval (Supplementary Information section 5). **l**, Size of $\mathbf{q}_{\text{Kekulé}}$ normalized by the size of the moiré reciprocal lattice vector \mathbf{g}_3 , which is almost aligned with $\mathbf{q}_{\text{Kekulé}}$. Error bars are set by the pixel size in **b–g** (Methods). The black dashed line shows the MBZ boundary.

exact position of the graphene reciprocal lattice vectors \mathbf{G}_1 , \mathbf{G}_2 and \mathbf{G}_3 . Next, based on these vectors, we can accurately estimate the positions of the Fourier transform peaks that would arise for a uniform Kekulé pattern on the graphene scale as $\mathbf{K}_1 = (\mathbf{G}_1 + \mathbf{G}_2)/3$, $\mathbf{K}_2 = (\mathbf{G}_2 + \mathbf{G}_3)/3$ and $\mathbf{K}_3 = (\mathbf{G}_3 - \mathbf{G}_1)/3$ (Fig. 4e–g, blue circles). None of the satellite peaks in the Fourier transform signal line up with \mathbf{K}_1 , \mathbf{K}_2 and \mathbf{K}_3 , although crucially, the observed displacement of all three sets of peaks relative to \mathbf{K}_1 , \mathbf{K}_2 and \mathbf{K}_3 can be accounted for by a single wavevector $\mathbf{q}_{\text{Kekulé}}$.

The extracted Kekulé modulation wavevector $\mathbf{q}_{\text{Kekulé}}$ does not change with V_{Bias} but evolves monotonically with V_{Gate} and is generally

incommensurate with the moiré potential. On hole doping from $\nu = -2$ to -2.5 , $\mathbf{q}_{\text{Kekulé}}$ always points along the \mathbf{g}_3 moiré reciprocal lattice vector within error bars (Fig. 4i) but increases in magnitude, eventually crossing the moiré Brillouin zone (MBZ) boundary near the commensurate point $\mathbf{g}_3/2$ (Fig. 4l). Note that these results are consistent with the real-space auto-correlation analysis in Fig. 3. Furthermore, the observed modulation is quite robust to magnetic fields. By performing similar mappings in moderate (2 T) and high (8 T) out-of-plane magnetic fields, we find that spatially varying Kekulé distortions are still present (Extended Data Fig. 5) and that $\mathbf{q}_{\text{Kekulé}}$ only slightly shifts

its direction from its zero field value. Finally, our procedure gives consistent results for $\mathbf{q}_{\text{Kekulé}}$ for maps with different sizes and taken at various V_{Bias} .

Discussion

We now discuss the implications of our observations for the nature of the correlated state between $\nu = -2$ and -2.5 . The identification of a Kekulé pattern modulating slowly with a generally incommensurate, doping-dependent wavevector suggests the presence of an IKS order. Theoretically, the IKS state arises out of an inter-valley nesting instability at a single wavevector \mathbf{q}_{IKS} in the presence of a small heterostrain (about 0.1–0.2%)^{3,4,27}—comparable to the values of our MATTG samples. The resulting order yields a lattice-tripling pattern that slowly varies between moiré lattice sites with wavelength $2\pi/|\mathbf{q}_{\text{IKS}}|$ along a direction set by \mathbf{q}_{IKS} (see Fig. 4h and Supplementary Information for more discussion and theoretical modelling). This vector is distinct from the extracted modulation wavevector $\mathbf{q}_{\text{Kekulé}}$. Whereas \mathbf{q}_{IKS} characterizes variations relative to the moiré lattice, $\mathbf{q}_{\text{Kekulé}}$ measures the modulation of the lattice-tripling order relative to the graphene lattice. The two vectors are related by a momentum shift that connects the moiré Brillouin zone centre $\boldsymbol{\gamma}$ and the moiré Brillouin zone corners $\boldsymbol{\kappa}$ (Fig. 4h).

Because the IKS order arises from an inter-valley nesting instability, it is greatly influenced by the structure of the flat bands³—especially the location of the flat-band maxima and minima at each valley. In the continuum model^{28,29}, the valence flat-band minima and maxima, respectively, occur at the moiré Brillouin zone $\boldsymbol{\gamma}$ and $\boldsymbol{\kappa}$, $\boldsymbol{\kappa}'$ points. On inclusion of heterostrain, these features are distorted in a non-universal fashion that depends on the strain angle and magnitude. Electronic interactions, which significantly alter the shape of the flat bands, are also crucial for determining the preferred IKS instability. Charge inhomogeneity, characterized by the self-consistent Hartree term, tends to invert the flat bands around the $\boldsymbol{\gamma}$ point^{30–35}. When interaction-induced band inversion is not pronounced, there is good agreement with the experiment. In this case, theoretically extracted $\mathbf{q}_{\text{Kekulé}}$ that includes measured heterostrain matches well with the observations, within the error bars of both the experimental extraction and the theoretical procedure (Supplementary Information). The calculated modulation wavevector $\mathbf{q}_{\text{Kekulé}}$ evolves with hole doping away from $\nu = -2$ following experimentally observed trends, with the evolution being more pronounced in the non-inverted regime. Incorporating a perpendicular displacement field induced by the back gate, which hybridizes the twisted bilayer graphene-like flat bands of MATTG with the Dirac cone (Supplementary Information section 2), leaves the theoretically extracted $\mathbf{q}_{\text{Kekulé}}$ largely unchanged (Supplementary Information Fig. 6). Finally, we note that the measured pattern in Fig. 3 seems to be very close to a commensurate modulation; see Supplementary Information section 9 for a possible mechanism favouring a lock-in of the IKS modulation to a nearby commensurate wavevector.

Our experiments show several other signatures directly related to symmetry breaking in MATTG. In many of the Fourier transform maps, we observed suppression of the Fourier transform satellite peaks along the narrow striped regions, forming a sash-like feature (Fig. 4a, white arrows) discussed theoretically in ref. 25 in the context of C_3 symmetry breaking (see also Extended Data Fig. 7). These sashes are resolved at various filling factors within both the graphene reciprocal lattice vector peaks and Kekulé peaks. Moreover, consistent with C_3 symmetry breaking on the graphene lattice scale, these sashes do not appear in all directions of the Fourier transform maps. This observation is compatible with the IKS ground state around $\nu = -2$. Similar features are observed near charge neutrality for $V_{\text{Gate}} = 0$ V, for which we did not detect lattice-tripling order. For this gate voltage, we further observed a preferred directionality in graphene bonds and a spatial evolution of the dI/dV signal near the AAA site that is consistent with a nematic semi-metallic ground state²⁵ (Extended Data Fig. 10).

These findings further highlight the ability of STM to distinguish various symmetry-broken ground states in moiré heterostructures.

Finally, our spectroscopic detection and characterization of IVC order provide insights into the puzzle surrounding the origin of superconductivity and the accompanying pseudogap phase in MATTG. The emergence of inter-valley coherence at fillings in which we previously reported unconventional superconductivity¹³ (Extended Data Fig. 9) constrains theoretical scenarios. Further constraints follow from the observation that the strength of the IVC order, quantified by the normalized Kekulé peak intensity, is maximum in the pseudogap regime (around $\nu \approx -2.3$ to -2.5), instead of in the $\nu = -2$ insulating phase. Other properties of MATTG have also been observed in this filling range, including the evolution from U- to V-shaped tunnelling spectra observed spectroscopically¹³, as well as a sharp change in the Ginzburg–Landau coherence length and maximum critical temperature observed in transit^{1,2}. Linking these diverse aspects of MATTG phenomenology poses a challenge for future theory and experiments. Another open question is how prevalent the IVC order among the strongly correlated graphene-based systems is as it is found not only in magic-angle bilayers¹⁵ and now trilayers but also in graphene at high magnetic fields^{19,20}.

Online content

Any methods, additional references, Nature Portfolio reporting summaries, source data, extended data, supplementary information, acknowledgements, peer review information; details of author contributions and competing interests; and statements of data and code availability are available at <https://doi.org/10.1038/s41586-023-06663-8>.

1. Park, J. M., Cao, Y., Watanabe, K., Taniguchi, T. & Jarillo-Herrero, P. Tunable strongly coupled superconductivity in magic-angle twisted trilayer graphene. *Nature* **590**, 249–255 (2021).
2. Hao, Z. et al. Electric field-tunable superconductivity in alternating-twist magic-angle trilayer graphene. *Science* **371**, 1133–1138 (2021).
3. Kwan, Y. H. et al. Kekulé spiral order at all nonzero integer fillings in twisted bilayer graphene. *Phys. Rev. X* **11**, 041063 (2021).
4. Wagner, G., Kwan, Y. H., Bultinck, N., Simon, S. H. & Parameswaran, S. A. Global phase diagram of the normal state of twisted bilayer graphene. *Phys. Rev. Lett.* **128**, 156401 (2022).
5. Fradkin, E., Kivelson, S. A. & Tranquada, J. M. *Colloquium: theory of intertwined orders in high temperature superconductors*. *Rev. Mod. Phys.* **87**, 457–482 (2015).
6. Fernandes, R. M. et al. Iron pnictides and chalcogenides: a new paradigm for superconductivity. *Nature* **601**, 35–44 (2022).
7. Zhang, Y. et al. Promotion of superconductivity in magic-angle graphene multilayers. *Science* **377**, 1538–1543 (2022).
8. Park, J. M. et al. Robust superconductivity in magic-angle multilayer graphene family. *Nat. Mater.* **21**, 877–883 (2022).
9. Kerelsky, A. et al. Maximized electron interactions at the magic angle in twisted bilayer graphene. *Nature* **572**, 95–100 (2019).
10. Choi, Y. et al. Electronic correlations in twisted bilayer graphene near the magic angle. *Nat. Phys.* **15**, 1174–1180 (2019).
11. Xie, Y. et al. Spectroscopic signatures of many-body correlations in magic-angle twisted bilayer graphene. *Nature* **572**, 101–105 (2019).
12. Jiang, Y. et al. Charge order and broken rotational symmetry in magic-angle twisted bilayer graphene. *Nature* **573**, 91–95 (2019).
13. Kim, H. et al. Evidence for unconventional superconductivity in twisted trilayer graphene. *Nature* **606**, 494–500 (2022).
14. Turkel, S. et al. Orderly disorder in magic-angle twisted trilayer graphene. *Science* **376**, 193–199 (2022).
15. Nuckolls, K. P. et al. Quantum textures of the many-body wavefunctions in magic-angle graphene. *Nature* **620**, 525–532 (2023).
16. Khalaf, E., Kruchkov, A. J., Tarnopolsky, G. & Vishwanath, A. Magic angle hierarchy in twisted graphene multilayers. *Phys. Rev. B* **100**, 085109 (2019).
17. Carr, S. et al. Ultraheavy and ultrarelativistic Dirac quasiparticles in sandwiched graphenes. *Nano Lett.* **20**, 3030–3038 (2020).
18. Gutiérrez, C. et al. Imaging chiral symmetry breaking from Kekulé bond order in graphene. *Nat. Phys.* **12**, 950–958 (2016).
19. Liu, X. et al. Visualizing broken symmetry and topological defects in a quantum Hall ferromagnet. *Science* **375**, 321–326 (2022).
20. Coissard, A. et al. Imaging tunable quantum Hall broken-symmetry orders in graphene. *Nature* **605**, 51–56 (2022).
21. Kang, J. & Vafeek, O. Strong coupling phases of partially filled twisted bilayer graphene narrow bands. *Phys. Rev. Lett.* **122**, 246401 (2019).
22. Bultinck, N. et al. Ground state and hidden symmetry of magic-angle graphene at even integer filling. *Phys. Rev. X* **10**, 031034 (2020).

23. Lian, B. et al. Twisted bilayer graphene. IV. Exact insulator ground states and phase diagram. *Phys. Rev. B* **103**, 205414 (2021).
24. Christos, M., Sachdev, S. & Scheurer, M. S. Correlated insulators, semimetals, and superconductivity in twisted trilayer graphene. *Phys. Rev. X* **12**, 021018 (2022).
25. Hong, J. P., Soejima, T. & Zaletel, M. P. Detecting symmetry breaking in magic angle graphene using scanning tunneling microscopy. *Phys. Rev. Lett.* **129**, 147001 (2022).
26. Călugăru, D. et al. Spectroscopy of twisted bilayer graphene correlated insulators. *Phys. Rev. Lett.* **129**, 117602 (2022).
27. Wang, T. et al. Kekulé spiral order in magic-angle graphene: a density matrix renormalization group study. Preprint at <https://doi.org/10.48550/arXiv.2211.02693> (2022).
28. Lopes dos Santos, J. M. B., Peres, N. M. R. & Castro Neto, A. H. Graphene bilayer with a twist: electronic structure. *Phys. Rev. Lett.* **99**, 256802 (2007).
29. Bistritzer, R. & MacDonald, A. H. Moiré bands in twisted double-layer graphene. *Proc. Natl Acad. Sci. USA* **108**, 12233–12237 (2011).
30. Guinea, F. & Walet, N. R. Electrostatic effects, band distortions, and superconductivity in twisted graphene bilayers. *Proc. Natl Acad. Sci. USA* **115**, 13174–13179 (2018).
31. Cea, T., Walet, N. R. & Guinea, F. Electronic band structure and pinning of Fermi energy to Van Hove singularities in twisted bilayer graphene: A self-consistent approach. *Phys. Rev. B* **100**, 205113 (2019).
32. Cea, T. & Guinea, F. Band structure and insulating states driven by Coulomb interaction in twisted bilayer graphene. *Phys. Rev. B* **102**, 045107 (2020).
33. Rademaker, L., Abanin, D. A. & Mellado, P. Charge smoothening and band flattening due to Hartree corrections in twisted bilayer graphene. *Phys. Rev. B* **100**, 205114 (2019).
34. Goodwin, Z. A. H., Vitale, V., Liang, X., Mostofi, A. A. & Lischner, J. Hartree theory calculations of quasiparticle properties in twisted bilayer graphene. *Electron. Struct.* **2**, 034001 (2020).
35. Xie, M. & MacDonald, A. H. Weak-field Hall resistivity and spin-valley flavor symmetry breaking in magic-angle twisted bilayer graphene. *Phys. Rev. Lett.* **127**, 196401 (2021).

Publisher's note Springer Nature remains neutral with regard to jurisdictional claims in published maps and institutional affiliations.

Springer Nature or its licensor (e.g. a society or other partner) holds exclusive rights to this article under a publishing agreement with the author(s) or other rightsholder(s); author self-archiving of the accepted manuscript version of this article is solely governed by the terms of such publishing agreement and applicable law.

© The Author(s), under exclusive licence to Springer Nature Limited 2023

Methods

Device fabrication

To fabricate the graphite/hBN/TTG device, the layers are first picked up sequentially using a poly(bisphenol A carbonate) film on a polydimethylsiloxane (PDMS) block using the typical dry transfer technique at temperatures between 60 °C and 100 °C. The stack then needs to be flipped onto a substrate to expose the TTG and needs to be electrically contacted without introducing polymer residues.

Stack flipping is accomplished using a gold-coated PDMS slide (Extended Data Fig. 1a–f). In this step, the poly(bisphenol A carbonate) film initially supporting the stack is peeled off of the PDMS slide and transferred stack-side down onto a PDMS block coated with Ti/Au (3/12 nm) using e-beam evaporation. The poly(bisphenol A carbonate) film is then removed using *N*-methyl-2-pyrrolidone (NMP). The gold surface and the stack are naturally sealed together, preventing the NMP from permeating the interface containing the TTG. Moreover, the evaporated metals prevent any residues from contacting the sample surface. Because the stiction between gold and the van der Waals stack is weaker than that between the van der Waals stack and silica, the stack can then be dropped onto an oxide substrate without the need for further solvent use.

To apply bias and gate voltages to the sample without contaminating the surface, we use a gold stamping technique (Extended Data Fig. 1g–k). First, an SU8 (SU-8 2005, Microchem) photoresist mould is defined on a silicon oxide substrate. Then, PDMS (SYLGARD 184, 10:1) is poured onto the mould and dried, resulting in a patterned stamp after peeling it off from the mould. Gold is evaporated (e-beam evaporation, 10–20 nm) onto the PDMS stamp, which is then pressed down onto the desired area of the sample at 130 °C. As only the highest parts of the stamp make contact with the sample—leaving the gold behind—the rest of the sample surface remains uncontaminated.

Samples B and C were prepared using our previously developed PDMS-assisted flipping technique¹⁰. The hBN/MATTG stack is picked up using a poly(bisphenol A carbonate) film, peeled off and flipped onto an intermediate PDMS block. The poly(bisphenol A carbonate) film is then washed away with NMP/isopropyl alcohol and kept under a vacuum for several days. The stack is subsequently transferred onto a graphite gate that has been previously dropped on a substrate. Finally, a graphite contact is exfoliated on PDMS and dropped to connect MATTG with a pre-patterned electrode.

To compare the quality of sample A with that of sample B, we used atomic force microscopy (AFM) in a.c. tapping mode (Extended Data Fig. 2). Sample B showed residues on the surface, which became apparent after scanning (cleaning) the area in contact mode because of the appearance of square residue boundaries. However, no signs of residues were observed on sample A before or after scanning the area in contact mode. Once a sample was fabricated, no further annealing was conducted inside the STM chambers.

Conductive AFM characterization at room temperature

Conductive AFM (CAFM) is a powerful imaging technique used for visualizing moiré patterns in twisted heterostructures, as reported in various studies^{36,37}. We used CAFM to characterize the twist angles and cleanliness of a sample at room temperature before cooling it down for STM measurements. A commercial AFM (Asylum Research Cypher) equipped with a conducting tip (ASYELEC-01-R2 from Asylum Research, with a spring constant of approximately 2.8 N m⁻¹) is used. During CAFM imaging, a bias voltage of 100 mV was typically applied between the tip and the twisted graphene, while the gate was left floating. The typical MATTG sample exhibits a moiré pattern surrounded by supermoiré stripes, as previously reported in the literature¹³ (Extended Data Fig. 2c,f). The region with a moiré wavelength of approximately 9 nm, which corresponds to the magic angle of TTG, was the target during the navigation of the STM tip to the sample.

STM measurements

The STM measurements were performed in a Unisoku USM1300J STM/AFM system using a Pt/Ir tip as in our previous works on bilayers^{38,39}. All reported features are observed with many (usually at least 10) different microtips. Unless specified otherwise, data were taken at temperature $T = 2$ K and the parameters for dI/dV spectroscopy measurements were $V_{\text{Bias}} = 100$ mV and $I = 1$ nA, and the lock-in parameters were modulation voltage $V_{\text{mod}} = 0.2$ –1 mV and frequency $f = 973$ Hz. Real-space dI/dV maps are taken with the constant height mode (feedback turned off, tilt corrected). The piezo scanner is calibrated on a Pb(110) crystal and verified by measuring the distance between the carbon atoms. The twist-angle uncertainty is approximately $\pm 0.01^\circ$ and is determined by measuring moiré wavelengths from topography. Filling-factor assignment has been performed by taking Landau fan diagrams as discussed previously³⁸ or by identifying features corresponding to full-filling and charge neutrality point LDOS suppression¹⁰ in datasets for which magnetic field dependence was not studied. The deviations between the two methods in assigning filling factors are typically within 5%.

The gate-tunable Kekulé reconstruction has been observed in all the studied areas in three different samples, including the sample in which we previously studied superconductivity¹³ (labelled sample C in this work). The large areas (that include more than 20 moiré sites) needed for unambiguously establishing the IKS order using Fourier transform analysis outlined in Fig. 4 were studied in sample A and discussed in the main text. The presence of inter-valley coherence is also confirmed in the sample with a larger heterostrain (sample B). The STM parameters used to measure various dI/dV maps are provided in Extended Data Table 1.

Heterostrain extraction

The presence of heterostrain deforms the moiré lattice from an ideal equilateral triangular lattice. By experimentally measuring the two moiré lattice vectors \mathbf{g}_1 and \mathbf{g}_2 , we can extract the magnitude and direction of the heterostrain that best match the observed moiré lattice geometry⁹ (see also Supplementary Information section 3 for details of strain modelling). The magnitude of the heterostrain is uniquely determined from the moiré lattice constants l_1 , l_2 and l_3 labelled in Fig. 1b—we obtain a magic angle of $1.60^\circ \pm 0.01^\circ$ and a strain magnitude of $|\epsilon| = (0.12 \pm 0.04)\%$. We note that twist angle and strain were extracted using large uniform areas (typically at least 30 nm \times 30 nm) containing tens of moiré sites. This minimizes any errors that could potentially arise from imperfections because of the piezo scanner tube (for example, the piezo creep effect).

The extraction of the strain direction is also sensitive to the twist-angle direction (clockwise versus anticlockwise), as well as which layer experiences compressive strain. In our experiment, we stacked the TTG such that the middle layer is rotated anticlockwise with respect to the top and bottom layers. We then extract the direction of the moiré lattice vectors \mathbf{g}_1 and \mathbf{g}_2 by comparing them with an armchair direction of graphene, or equivalently to the \mathbf{G}_1 vector in the Fourier transform. This information lets us conclude that the middle layer experiences compressive strain (corresponding to negative ϵ in our conventions). With these extra pieces of information, the strain magnitude $\epsilon = -(0.12 \pm 0.04)\%$ and strain angle $\varphi = (87 \pm 10)^\circ$ are extracted. The same method has been used for sample B and sample C. From sample B, we got strain magnitude $\epsilon = -(0.28 \pm 0.04)\%$ and strain angle $\varphi = (138 \pm 10)^\circ$. From sample C, we got strain magnitude $\epsilon = -(0.11 \pm 0.04)\%$ and strain angle $\varphi = (60 \pm 10)^\circ$.

Kekulé auto-correlation analysis

Variation of the Kekulé pattern on the neighbouring AAA sites is quantified by calculating the correlation between two small images taken at two spatially different parts of the large dI/dV map. The correlation, which we define as an element-wise multiplication between

Article

two same-sized images, is normalized such that it gives 1 for two identical images and -1 for fully reversed images. A two-dimensional auto-correlation map plots the correlation between a fixed window, centred at a particular AAA site, and a moving window that spans the whole dI/dV map. The size of the window we choose to calculate the auto-correlation map in Fig. 3h is 1.2 nm; the result is insensitive to the size of the window within 0.8–1.7 nm.

A Kekulé dI/dV auto-correlation map calculates the correlation in a Fourier-transform-filtered dI/dV map that contains only signals that are periodic with the Kekulé wavevector. Fourier transform filtering is performed by first identifying six peaks corresponding to Kekulé distortion (\mathbf{K}_i) and six peaks for graphene reciprocal lattice vectors (\mathbf{G}_i). Six round masks of radius 3.5 nm^{-1} centred on Kekulé (graphene) Fourier transform peaks are used to separate the desired signal from the rest of the data. A Fourier-transform-filtered dI/dV map is produced by performing an inverse Fourier transform on a masked Fourier transform image. We calculate auto-correlation on the Fourier-transform-filtered Kekulé dI/dV maps and plot only those peaks that are at local maxima in the graphene dI/dV auto-correlation map to trace the evolution of auto-correlation only when the two windows are atomically aligned.

Extraction of IKS wavevector

Because the IKS ground state is constructed by hybridizing the K and K' valleys with a momentum mismatch \mathbf{q}_{IKS} , Fourier transform peaks appear at $\mathbf{Y} - \mathbf{Y}' - \mathbf{q}_{\text{IKS}}$ or equivalently at $\mathbf{k}_{\text{top}} - \mathbf{k}'_{\text{top}} - \mathbf{q}_{\text{Kekulé}}$, rather than $\mathbf{k}_{\text{top}} - \mathbf{k}'_{\text{top}}$ for uniform Kekulé distortion (Fig. 4h). We extract the IKS wavevector \mathbf{q}_{IKS} or equivalently $\mathbf{q}_{\text{Kekulé}}$ by measuring how much the Fourier transform peaks are offset from $\mathbf{k}_{\text{top}} - \mathbf{k}'_{\text{top}}$. Although in theory, the vector $\mathbf{k}_{\text{top}} - \mathbf{k}'_{\text{top}}$ can be easily deduced from graphene reciprocal lattice vector peaks in the Fourier transform, small uncertainty in piezo calibration and the effect of strain makes it hard to distinguish the central graphene reciprocal lattice vector peak among many satellite peaks with similar intensities. Although neighbouring satellite peaks at \mathbf{G}_i are separated by one moiré reciprocal lattice vector \mathbf{g} , their high-order counterparts at $n\mathbf{G}_i$ are apart by $n\mathbf{g}$. If our choice of exact \mathbf{G}_i is off by \mathbf{g} , the exact $3\mathbf{G}_i$ will be located $3\mathbf{g}$ away from the current \mathbf{G}_i (Extended Data Fig. 6, yellow circle), which is unlikely considering that the prominent satellite peaks are located within $\pm 2\mathbf{g}$ from the centre of the cluster. Our choice of \mathbf{G}_1 and \mathbf{G}_2 in Fig. 4b,c is the only choice that yields high-order Fourier transform peaks at $m\mathbf{G}_1 + n\mathbf{G}_2$ (where m and n are integers from -3 to $+3$); \mathbf{G}_3 is automatically determined by $\mathbf{G}_3 = \mathbf{G}_2 - \mathbf{G}_1$ because we have only two independent reciprocal lattice vectors. The plotted \mathbf{G}_3 (Fig. 4d, black circle) is precisely on top of a Fourier transform peak, consistent with the fact that we do not observe other long-wavelength patterns in Fourier-transform-filtered graphene dI/dV maps. Once we determine which Fourier transform peak corresponds to the exact \mathbf{G}_i , the naively expected Kekulé Fourier transform peak positions (which would occur for time-reversal-symmetric IVC order) are calculated as $\mathbf{K}_1 = (\mathbf{G}_1 + \mathbf{G}_2)/3$, $\mathbf{K}_2 = (\mathbf{G}_2 + \mathbf{G}_3)/3$ and $\mathbf{K}_3 = (\mathbf{G}_3 - \mathbf{G}_1)/3$. Note that any satellite Fourier transform peak can be chosen to calculate $\mathbf{q}_{\text{Kekulé}}$, which is defined as the momentum separation from the calculated \mathbf{K}_i up to a modulo moiré reciprocal lattice vector \mathbf{g} . Wavevectors are only defined modulo moiré reciprocal lattice vectors—which are precisely identified as the momentum distance between the satellite peaks observed in Fig. 4, and thus any choice of reference moiré peak will yield a physically equivalent result. A particular Fourier transform peak is chosen to calculate $\mathbf{q}_{\text{Kekulé}}$, so that the norm of $\mathbf{q}_{\text{Kekulé}}$ does not exceed the norm of \mathbf{g} and the gate dependence of $\mathbf{q}_{\text{Kekulé}}$ can be traced continuously. Also, three $\mathbf{q}_{\text{Kekulé}}$ can be extracted separately from \mathbf{K}_1 , \mathbf{K}_2 and \mathbf{K}_3 , and all three values match within the experimental range of error.

Kekulé wavevector error comes from locating the exact centre of the Fourier transform peak with a finite width, which has intrinsic uncertainties coming from the measurement resolution and error due to the broadening of the peaks because of structural inhomogeneity. By taking

a much larger map in the same area ($150 \text{ nm} \times 150 \text{ nm}$, not shown), we verified that Fourier transform peaks are not limited by the structural inhomogeneity and set by the measurement resolution. We estimate the error bars in Fig. 4i, $\Delta \mathbf{q}_{\text{Kekulé}} \approx \sqrt{2} \times 0.09 \text{ nm}^{-1} = 0.12 \text{ nm}^{-1}$, where 0.09 nm^{-1} is half of the pixel size in Fig. 4b–g.

Inter-valley coherence in MATTG and other graphene-based systems

Although many twisted graphene-based platforms have been proposed so far, the family of alternating-twist multilayers (including twisted bilayer graphene and TTG) stand out because of their common set of symmetries and similar experimental phenomenology. In this context, the observation of the IVC order in MATTG can be understood to originate from the flat-band sector of the twisted-bilayer-graphene-like bands (Supplementary Information). We note, however, that because of the smaller moiré unit cell, the effect of strain and correlations in the two systems slightly differ, and consequently, the direct comparison of Kekulé reconstruction details and its doping dependence here and in ref. 15 may not be straightforward. In a more general context of moiré structures, apart from magic-angle twisted bilayer graphene, the structure of the flat bands in other moiré systems can be very different, and as such, it is an interesting open question for future investigations if the IVC order is established in those systems as well. Finally, we note that recently IVC is also reported in monolayer graphene placed in high magnetic fields. At first glance, the phenomenology, in general, is similar to the moiré systems as both platforms exhibit spontaneous breaking of valley-charge conservation because of strong electronic interactions, but the monolayer graphene experiment is different in several ways. The most important is that it takes place in the quantum Hall regime, in which the non-interacting theory is described by Landau levels, and the time-reversal symmetry is broken.

Data availability

The raw data shown in the main figures are available at Zenodo (<https://doi.org/10.5281/zenodo.8317363>). Other data that support the findings of this study are available from the corresponding authors upon reasonable request.

Code availability

The code that supports the findings of this study is available from the corresponding authors upon reasonable request.

36. Zhang, S. et al. Abnormal conductivity in low-angle twisted bilayer graphene. *Sci. Adv.* **6**, eabc5555 (2020).
37. Huang, X. et al. Imaging dual-Moiré lattices in twisted bilayer graphene aligned on hexagonal boron nitride using microwave impedance microscopy. *Nano Lett.* **21**, 4292–4298 (2021).
38. Choi, Y. et al. Correlation-driven topological phases in magic-angle twisted bilayer graphene. *Nature* **589**, 536–541 (2021).
39. Choi, Y. et al. Interaction-driven band flattening and correlated phases in twisted bilayer graphene. *Nat. Phys.* **17**, 1375–1381 (2021).

Acknowledgements We thank N. Bultinck, S. Parameswaran, A. Pasupathy, A. Vishwanath, S. Todadri and A. Yazdani for the discussions. We are grateful in particular to T. Soejima and M. Zaletel for pointing out subtleties regarding the extraction of \mathbf{q}_{IKS} through Fourier analysis. This work has been primarily supported by the National Science Foundation (grant no. DMR-2005129); the Office of Naval Research (grant no. N142112635); and the Army Research Office (grant award W911NF17-1-0323). S.N.-P. acknowledges support from the Sloan Foundation. J.A. and S.N.-P. also acknowledge support from the Institute for Quantum Information and Matter, an NSF Physics Frontiers Center with support of the Gordon and Betty Moore Foundation (grant no. GBMF1250); É.L.-H. and C.L. acknowledge support from the EPIQS Initiative of the Gordon and Betty Moore Foundation (grant no. GBMF8682) (at Caltech). C.L. acknowledges start-up funds from the Florida State University and the National High Magnetic Field Laboratory. The National High Magnetic Field Laboratory is supported by the National Science Foundation through NSF/DMR-1644779 and the state of Florida. A.T. and J.A. are grateful for the support of the Walter Burke Institute for Theoretical Physics at Caltech. H.K. acknowledges support from the Kwanjeong fellowship. L.K. acknowledges support from an IQIM-AWS Quantum postdoctoral fellowship. The primary support for sample fabrication

efforts at UCSB was provided by the US Department of Energy (award no. DE-SC0020305). This work used facilities supported by the UC Santa Barbara NSF Quantum Foundry funded by the Q-AMASE-i programme under award DMR-1906325.

Author contributions H.K. and Y.C. fabricated samples with the help of Y.Z., H.Z. and L.H. and performed STM measurements. H.K., Y.C. and S.N.-P. analysed the data with the help of L.K. and E.B. É.L.-H., C.L. and A.T. provided the theoretical analysis supervised by J.A. S.N.-P. supervised the project. K.W. and T.T. provided the hBN crystals and A.F.Y. supervised the device fabrication efforts. H.K., Y.C., É.L.-H., C.L., A.T., J.A. and S.N.-P. wrote the paper with input from other authors.

Competing interests The authors declare no competing interests.

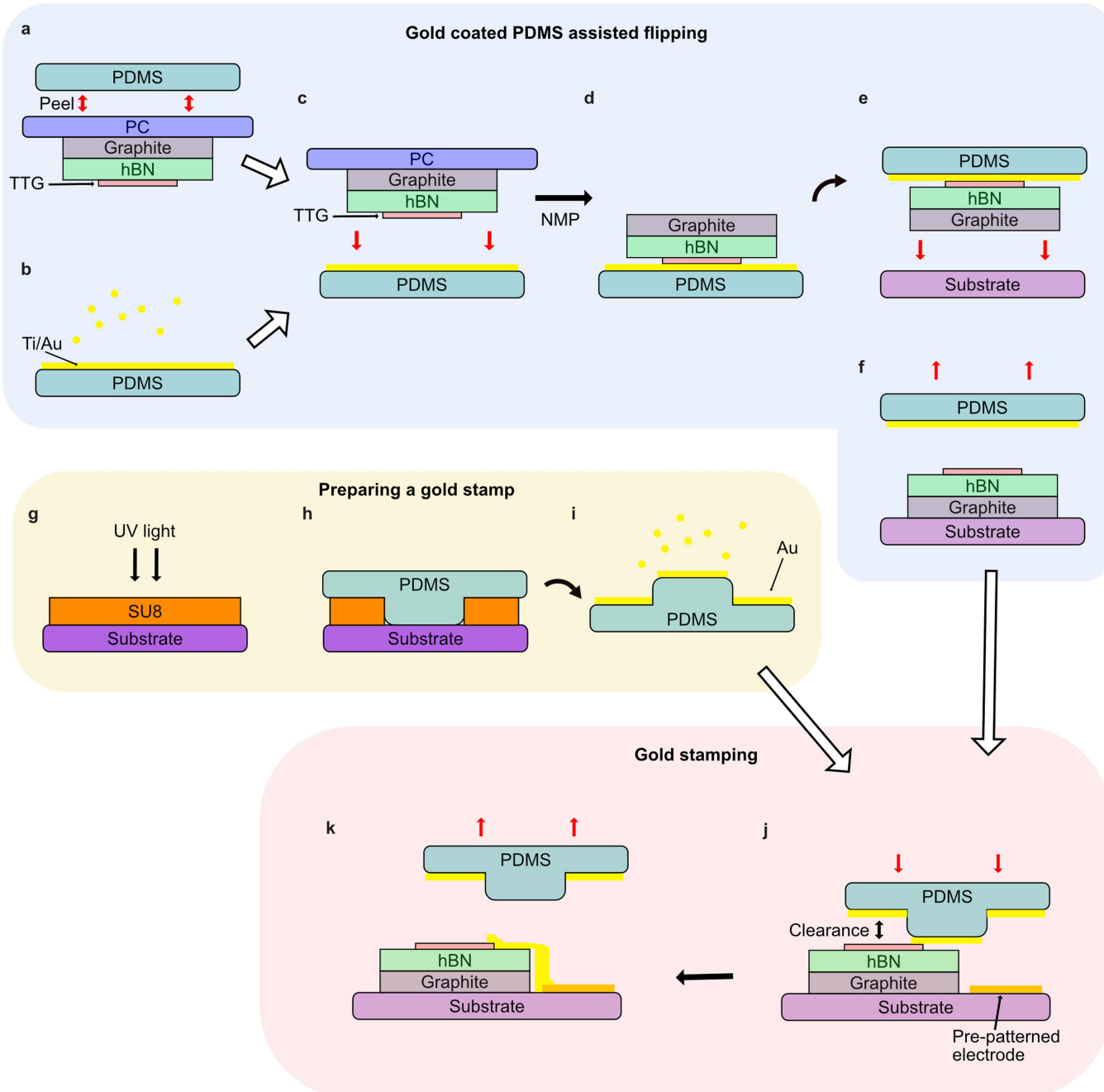
Additional information

Supplementary information The online version contains supplementary material available at <https://doi.org/10.1038/s41586-023-06663-8>.

Correspondence and requests for materials should be addressed to Hyunjin Kim or Stevan Nadj-Perge.

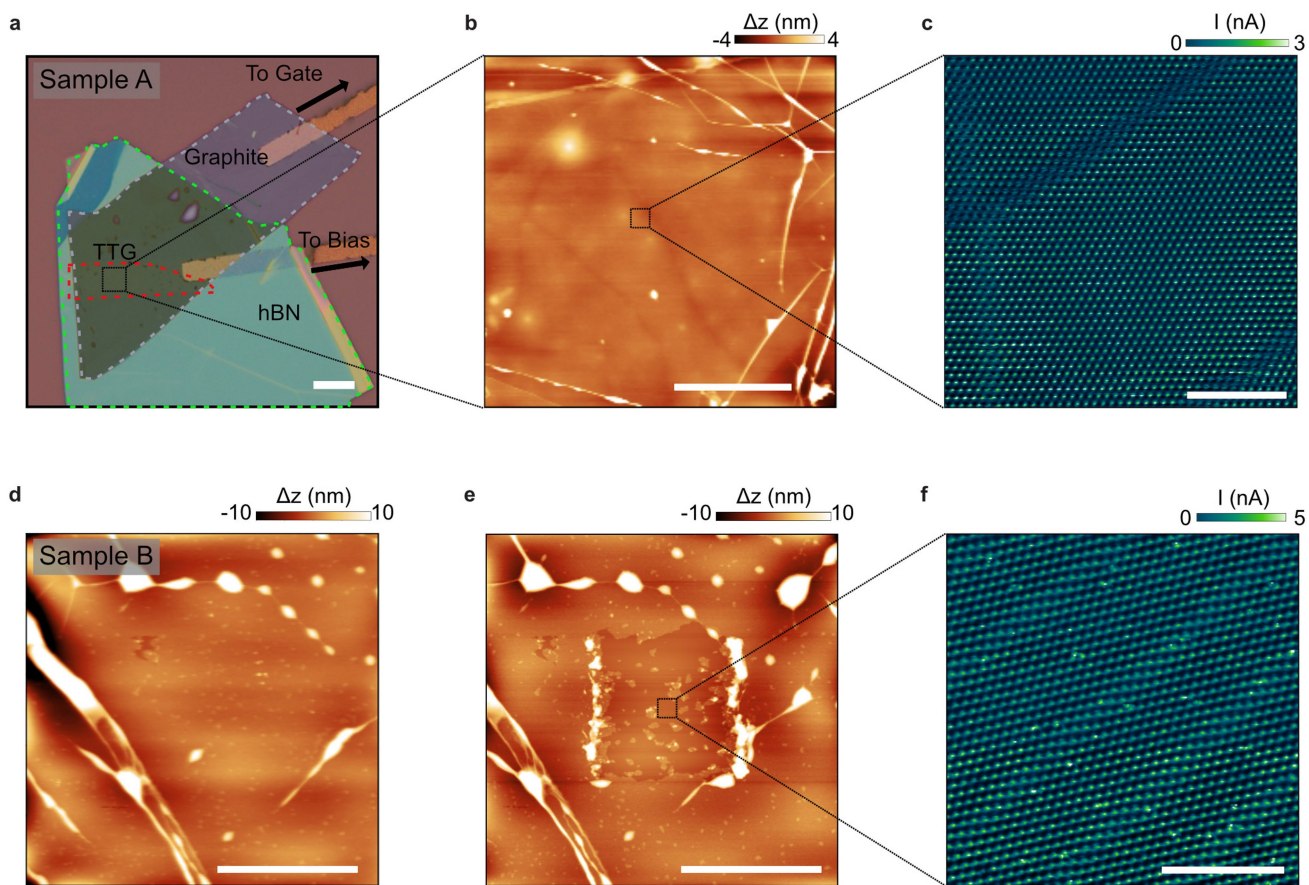
Peer review information *Nature* thanks Peter Nemes-Incze, Xiao Yan Xu and Long Jing Yin for their contribution to the peer review of this work.

Reprints and permissions information is available at <http://www.nature.com/reprints>.



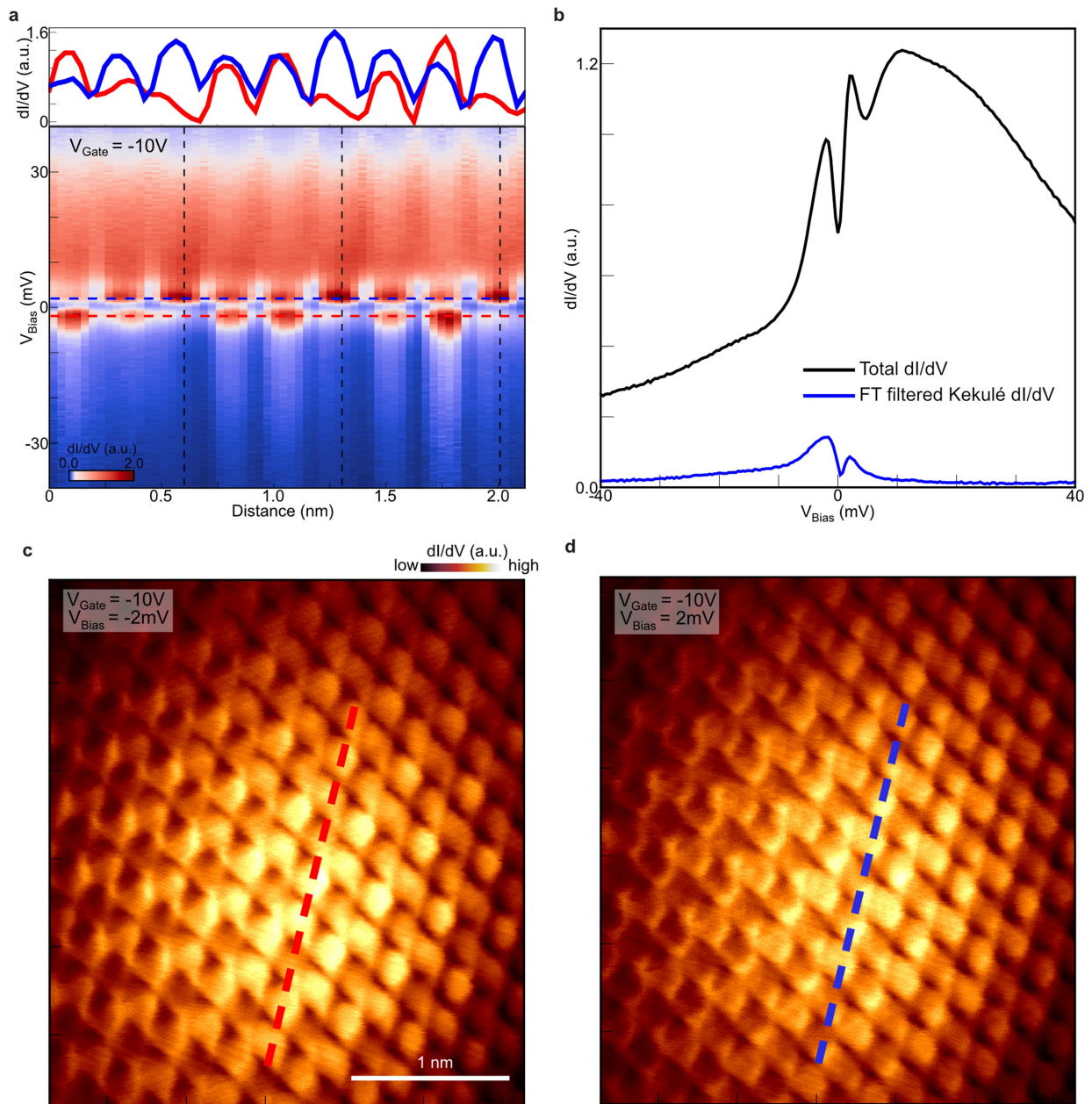
Extended Data Fig. 1 | Sample fabrication. **a-f**, Gold coated PDMS assisted flipping. A stack with PC film is peeled off from a PDMS block (**a**). A separate PDMS block is Ti/Au coated (**b**). Then the stack is put down to the gold coated PDMS (**c**). PC film is dissolved by NMP (**d**), before the stack is dropped down to a substrate (**e,f**). **g-i**, A gold stamp is prepared. A mould is defined by

photolithography (**g**). PDMS is poured on the mould (**h**), and peeled off. Au is deposited on the stamp (**i**). **j,k**, The gold stamp is pressed down onto a desired area of the sample (**j**), leaving a gold strip that connects the sample and a pre-patterned electrode on the substrate (**k**).



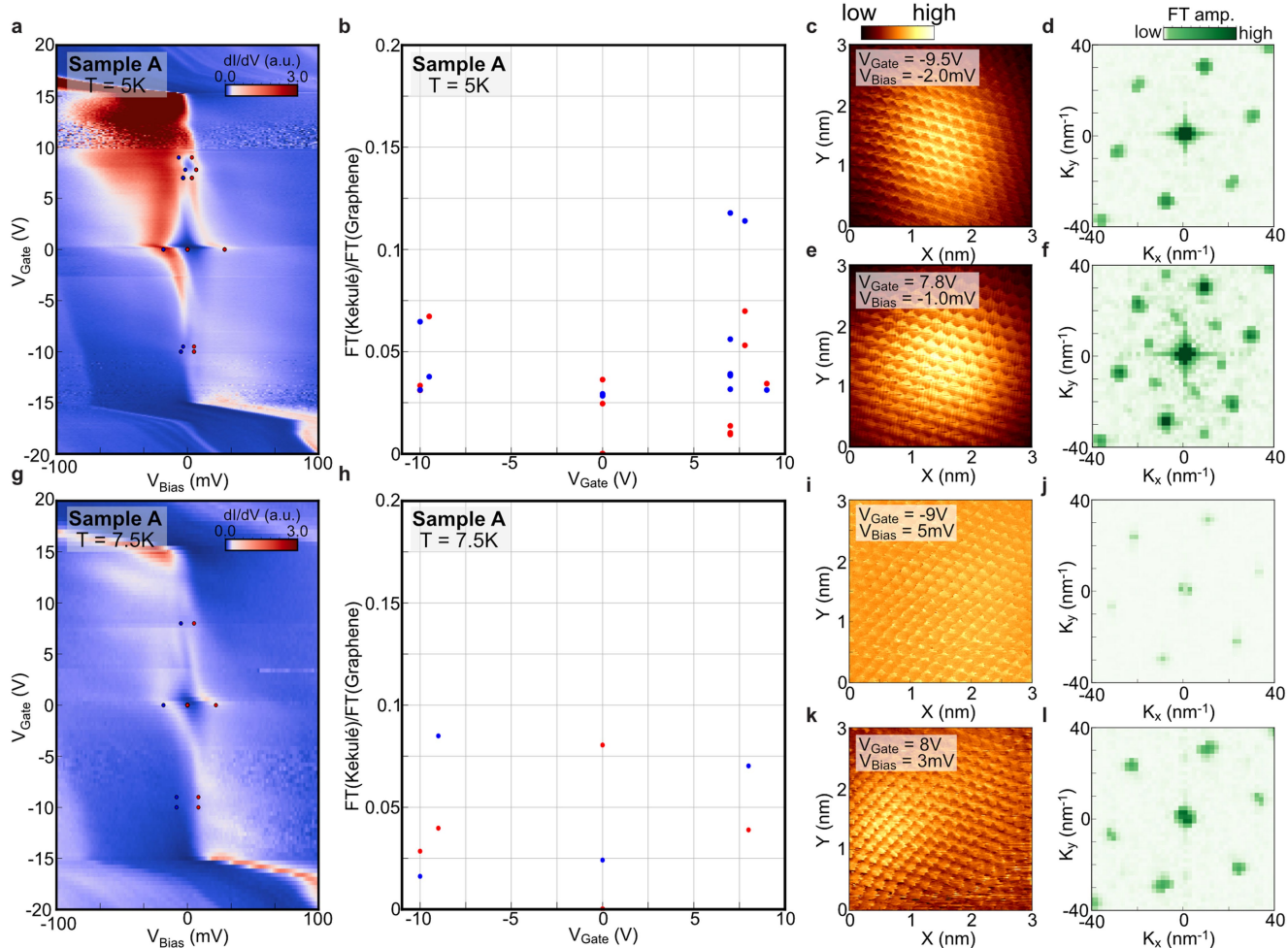
Extended Data Fig. 2 | AFM images of samples A and B. **a**, Optical microscope image of Sample A. **b**, AC tapping mode AFM image after the contact mode cleaning the $2 \times 2 \mu\text{m}^2$ area around the centre of the image. No sign of residue is found. **c**, cAFM image showing moiré pattern of MATTG. **d,e**, AC tapping mode

AFM images of Sample B before (**d**) and after (**e**) cleaning. The residue boundaries after the cleaning indicate significant amount of residues on the surface. **f**, cAFM image. Scale bars: $10 \mu\text{m}$ (**a**), $2 \mu\text{m}$ (**b,d,e**), 100nm (**c,f**).



Extended Data Fig. 3 | V_{Bias} dependent mapping of the lattice tripling order on MATTG. **a.** Conductance at $V_{Gate} = -10V$ taken along spatial points and for range of V_{Bias} . While at large positive V_{Bias} , dI/dV shows periodic modulation that corresponds to graphene lattices, at low V_{Bias} , additional periodic pattern that triples the graphene lattice periodicity is apparent (black dashed lines). Upper inset shows two linecuts taken at above ($V_{Bias} = 2mV$) and below ($V_{Bias} = -2mV$) E_F stressing lattice tripling. **b.** V_{Bias} spectroscopy extracted from Extended Data

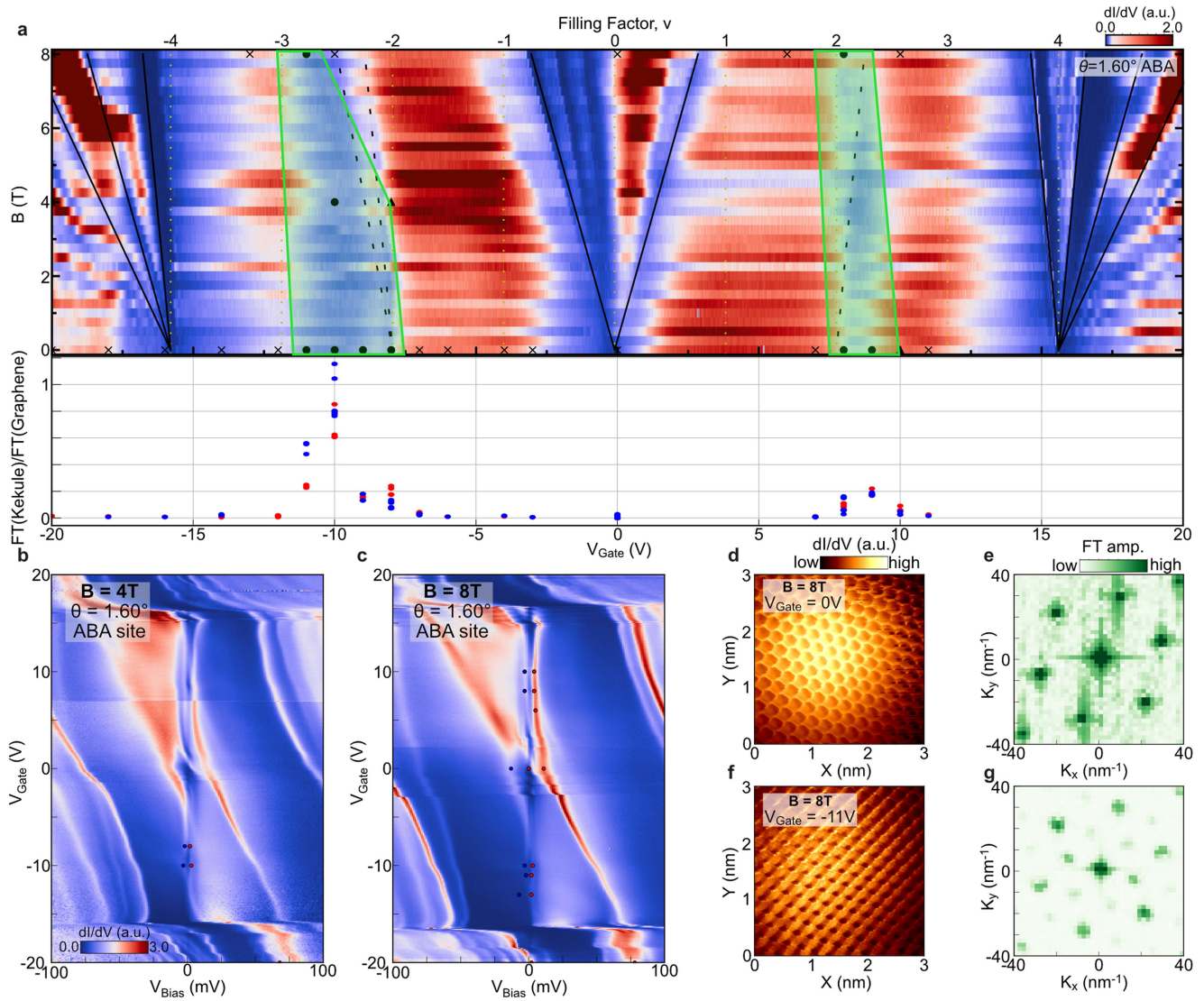
Fig. 3a that compares total dI/dV obtained by summing up along spatial coordinates and FT filtered Kekulé dI/dV which is a result of FT filtering on Extended Data Fig. 3a along spatial direction to extract Kekulé signal. **c,d.** dI/dV map measured at fixed $V_{Gate} = -10V$ at negative $V_{Bias} = -2mV$ (**c**) and positive $V_{Bias} = 2mV$ (**d**). Red and blue dashed line shows the spatial positions where Extended Data Fig. 3a is measured. Measurements are taken at $T = 400mK$.



Extended Data Fig. 4 | V_{Gate} dependent evolution of the lattice tripling order at higher temperatures.

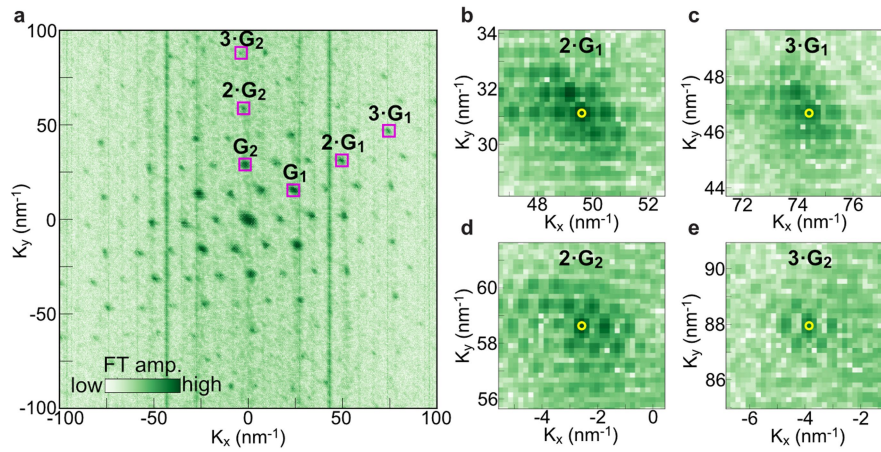
a, V_{Gate} dependent dI/dV spectroscopy measured at $T = 5\text{K}$ where $\nu = 2$ correlated gap survives but gaps around $\nu = -2$ is greatly suppressed. Red (positive V_{Bias}) and blue (negative V_{Bias}) dots marks the position where we measured 2D dI/dV maps. **b**, Intensity of the peak at Kekulé reciprocal lattice vector normalized by the intensity of the peak at graphene reciprocal lattice vector as a function of V_{Gate} . **c, e**, Real space dI/dV map at $V_{\text{Gate}} = -9.5\text{V}$ (**c**) and $V_{\text{Gate}} = 7.8\text{V}$ (**e**). **d, f**, Fourier transformation of Extended Data Fig. 4c, e.

g, V_{Gate} dependent dI/dV spectroscopy measured at $T = 7.5\text{K}$ where $\nu = 2$ correlated gap survives but gaps around $\nu = -2$ are greatly suppressed. Red (positive V_{Bias}) and Blue (negative V_{Bias}) dots mark the position where we measured 2D dI/dV maps. **h**, Intensity of the peak at Kekulé reciprocal lattice vector normalized by the intensity of the peak at graphene reciprocal lattice vector as a function of V_{Gate} . **i, j**, Real space dI/dV map at $V_{\text{Gate}} = -9.5\text{V}$ (**i**) and $V_{\text{Gate}} = 7.8\text{V}$ (**j**). **k, l**, Fourier transformation of Extended Data Fig. 4k, l.



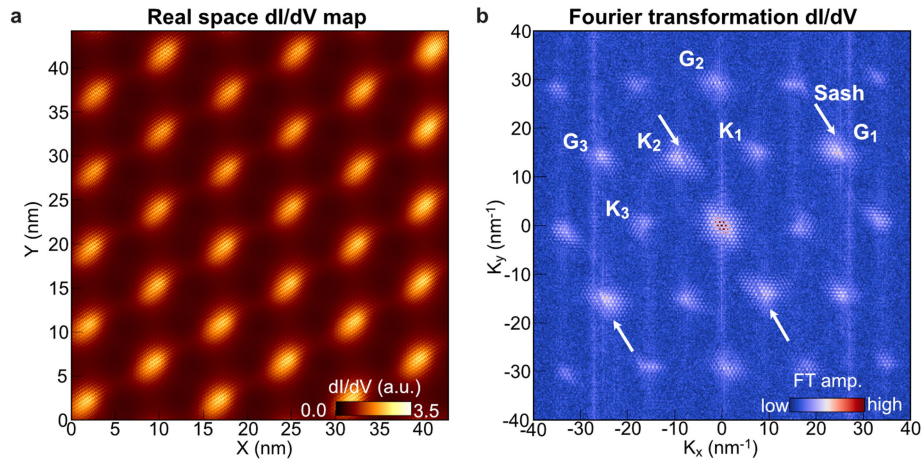
Extended Data Fig. 5 | Out-of-plane magnetic field dependence of lattice tripling order. **a**, LDOS Landau fan diagram measured on an moiré ABA site. The lower panel shows intensity of the lattice tripling signal as in Fig. 2. Black circles marked on Landau fan indicate V_{Gate} and B , where we observe Kekulé peaks in FT. The black cross indicate values of V_{Gate} and B where we measured dI/dV map but could not observe Kekulé peaks in FT. The green polygon is an

eye guide covering black circles and roughly denotes where we observed lattice tripling. **b, c**, V_{Gate} dependent dI/dV spectroscopy measured at $B = 4\text{ T}$ (**b**) and $B = 8\text{ T}$ (**c**). **d, e**, Real space dI/dV map (**d**) and corresponding Fourier transformation (**e**) showing the absence of Kekulé FT peaks around CNP at $B = 8\text{ T}$. **f, g**, Real space dI/dV map (**f**) and corresponding Fourier transformation (**g**) taken at $B = 8\text{ T}$ that shows Kekulé order at $V_{Gate} = -11\text{ V}$.

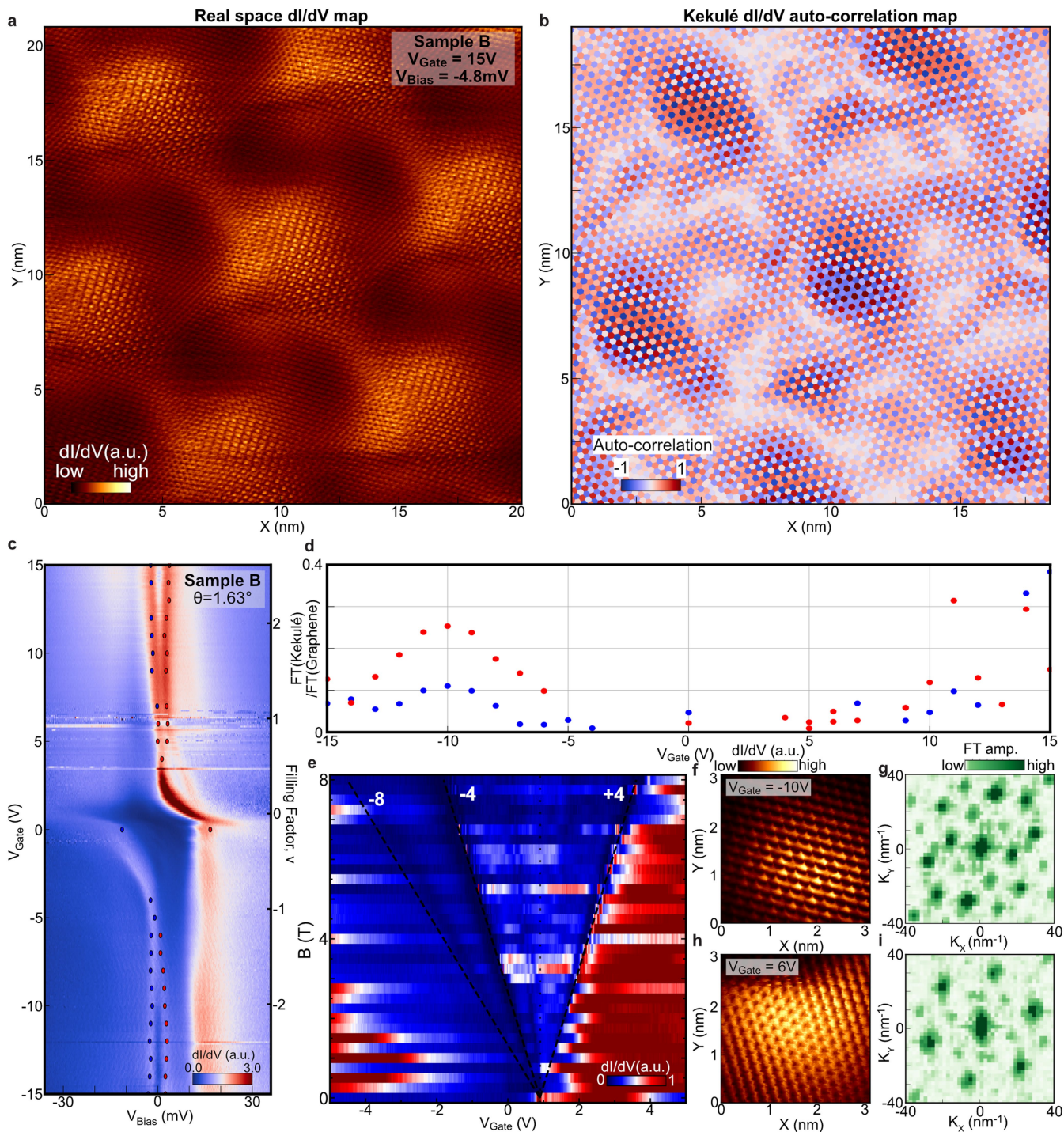


Extended Data Fig. 6 | High-order graphene reciprocal lattice vector peaks from FT map at $v = -2.3$. **a**, Fourier transformation of the real space dI/dV map at $V_{\text{gate}} = -9\text{V}$ and $V_{\text{bias}} = -2\text{mV}$ showing larger momentum range compared to Fig. 4a. **b-e**, Zoom-in of the Extended Data Fig. 6a around $2\mathbf{G}_1$ (**b**), $3\mathbf{G}_1$ (**c**), $2\mathbf{G}_2$ (**d**),

$3\mathbf{G}_2$ (**e**) that are marked by the violet rectangles in Extended Data Fig. 6a. Position of $N\mathbf{G}_i$ that is determined from the positions of \mathbf{G}_1 and \mathbf{G}_2 from Fig. 4b,c is plotted as yellow circles which matches well with the FT peaks.

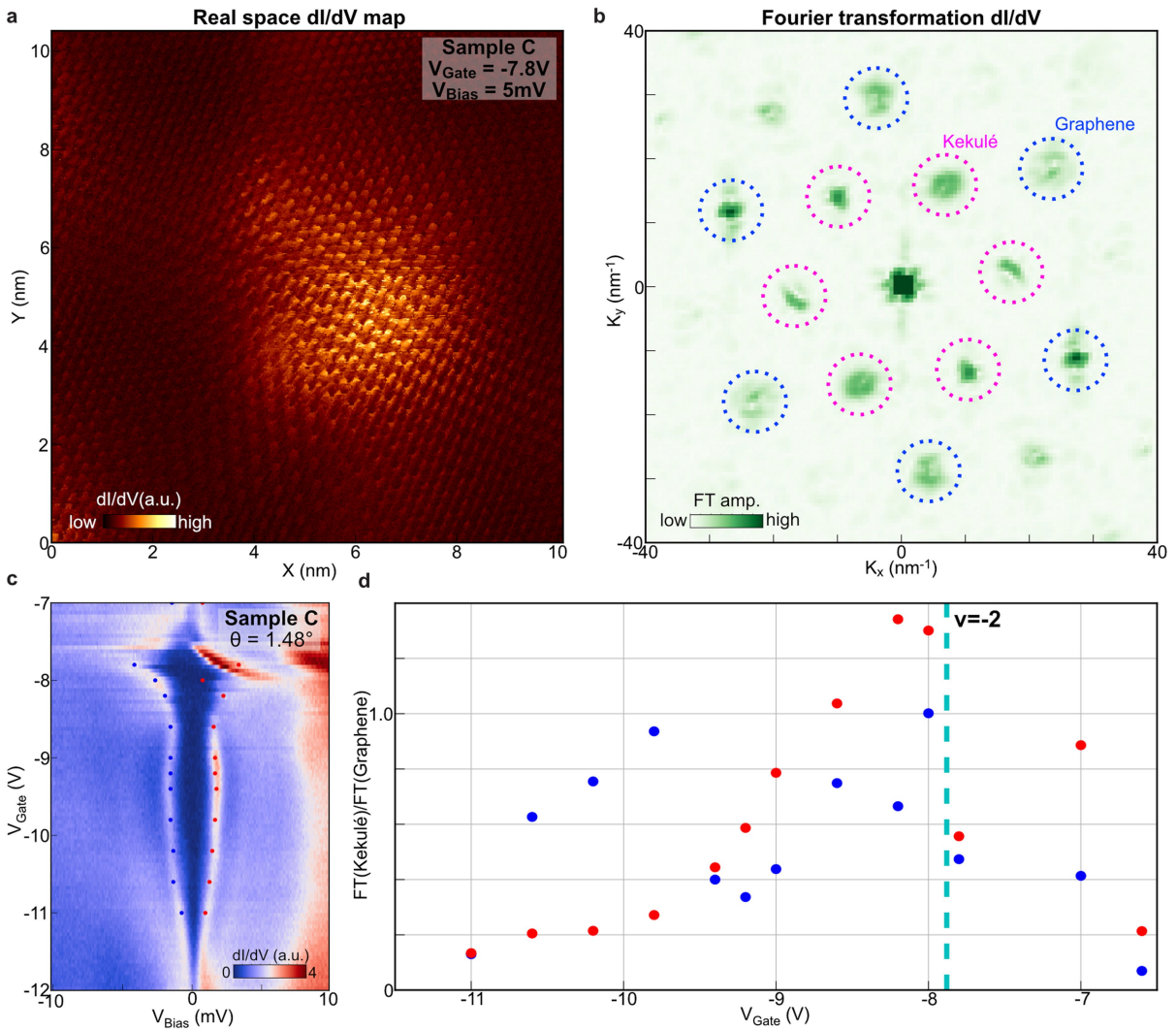


Extended Data Fig. 7 | 42 nm by 42 nm size dI/dV map with Fourier transformation at $\nu = -2.3$ showing sash features. a, b, Real space dI/dV map (a) and corresponding Fourier transformation (b) taken at $V_{\text{bias}} = -2\text{mV}$. White arrows point to the 'sash' features.



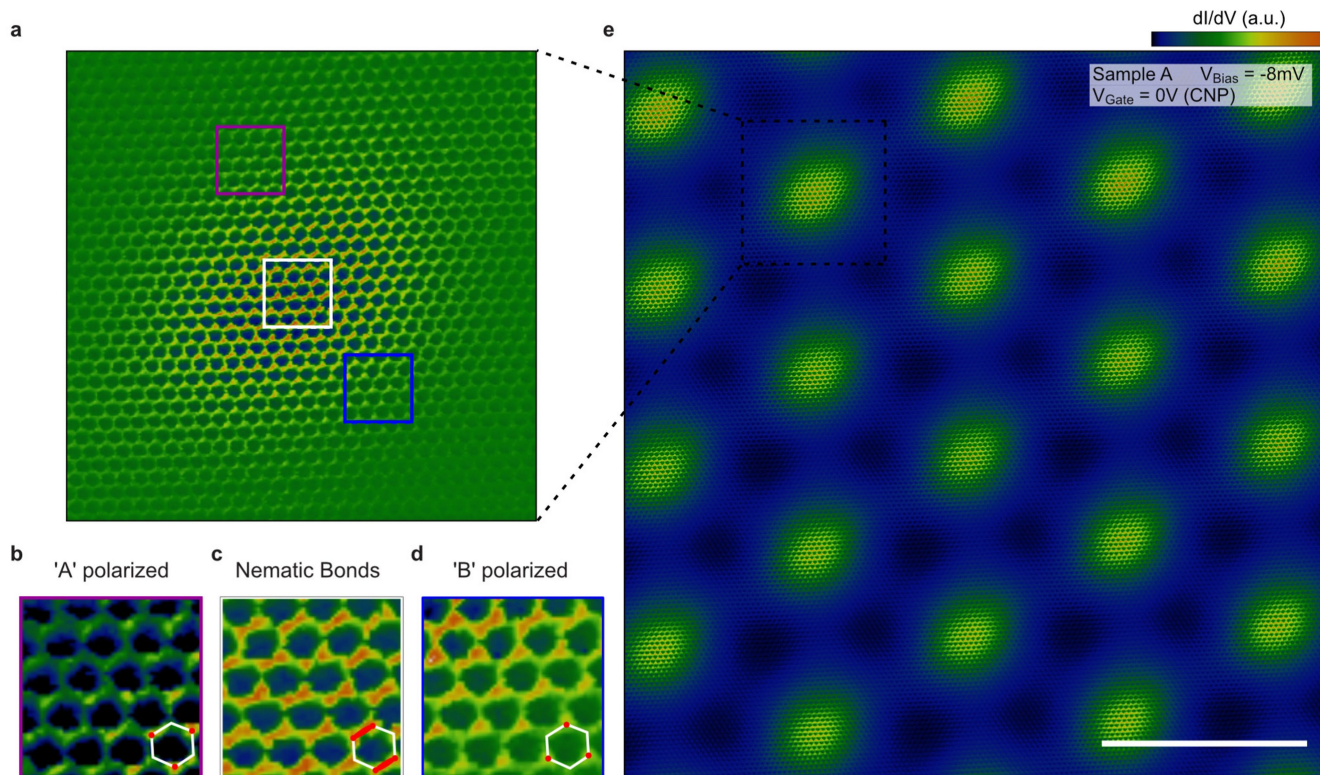
Extended Data Fig. 8 | Lattice tripling order observed in sample B. **a**, Real space dI/dV map taken at $V_{\text{Gate}} = 15\text{V}$ and $V_{\text{Bias}} = -4.8\text{mV}$ that includes seven moiré AAA sites. The area has twist angle of $\theta = 1.59^\circ$ and heterostrain of $\epsilon = 0.28\%$. **b**, Kekulé auto-correlation map created from real space dI/dV map in Extended Data Fig. 8a. Neighbouring AAA sites are mapped with different colours, exhibiting the change in Kekulé patterns. **c**, V_{Gate} dependent dI/dV spectroscopy measured on sample B. **d**, V_{Gate} dependence of the Kekulé peak intensity in FT

images normalized by the graphene lattice peak. Red (blue) dot corresponds to positive (negative) V_{Bias} , and is marked in Extended Data Fig. 8c. **e**, LDOS Landau fan diagram measured on sample B. Landau level degeneracies at each insulating dip is written in white numbers. **f, g**, Real space dI/dV map (**f**) and Fourier transformation (**g**) taken at $V_{\text{Gate}} = -10\text{V}$ showing lattice tripling. **h, i**, Real space dI/dV map (**h**) and Fourier transformation (**i**) taken at $V_{\text{Gate}} = 19\text{V}$. Measurements are taken at $T = 2\text{K}$.



Extended Data Fig. 9 | Lattice tripling order observed in sample C. **a**, Real space dI/dV map on one moiré AAA site measured at $V_{\text{Gate}} = -7.8\text{V}$ and $V_{\text{Bias}} = 5\text{mV}$ which is at $\nu = -2$. The area has twist angle of $\theta = 1.48^\circ$ and heterostrain of $\epsilon = 0.08\%$. **b**, Fourier transformation of Extended Data Fig. 9a exhibiting prominent Kekulé FT peaks. **c**, V_{Gate} dependent dI/dV spectroscopy focusing on

the correlated gaps at $\nu = -2$ - -3 . **d**, V_{Gate} dependence of the Kekulé peak intensity in FT images normalized by the graphene lattice peak. Measurements are taken at $T = 400\text{mK}$. In this sample, in the same area, we have previously established the presence of superconductivity¹³.



Extended Data Fig. 10 | Nematic semimetal phase at charge neutrality.
a, Atomic resolution dI/dV map (background filtered) at an AAA site.
b–d, Signatures of nematic semimetallic (NSM) ground state. The intensity of one bond is stronger than the other two bonds near the centre of the AAA site (c). The pattern slowly evolves into 'A' sublattice polarized state around the violet boxed region (b), while 'B' sublattice polarized state is dominant around

the blue boxed region (d), which agrees with the prediction in ref. 25.
e, (Unprocessed) dI/dV map at $V_{\text{Gate}} = 0\text{V}$ (CNP) on the hole side ($V_{\text{Bias}} = -8\text{mV}$) where **a–d** are taken. Other AAA sites in this map also show similar behaviour as **a–d**. This map and the map in Fig. 3 are taken at the same area, only having different gate and bias voltages. Scale bar : 10 nm.

Article

Extended Data Table 1 | Summary of V_{Bias} values used for the dI/dV maps in the main figures

Figure number	V_{Gate}	V_{Bias}
Fig. 2a	-20V	63mV
Fig. 2b	-10V	-3mV
Fig. 2c	0V	-13mV
Fig. 2d	9V	3mV
Fig. 3a	-9V	2mV
Fig. 4a	-9V	-2mV
Fig. 4i	-7.75V	-2mV
Fig. 4i	-8.3V	-2mV
Fig. 4i	-8.6V	-2mV
Fig. 4i	-9V	-2mV
Fig. 4i	-9V	2mV
Fig. 4i	-9.35V	-2mV
Fig. 4i	-9.7V	-2mV
Extended Data Fig. 5d	0V	11mV
Extended Data Fig. 5e	-11V	-2mV
Extended Data Fig. 6a-e	-9V	-2mV
Extended Data Fig. 7a-b	-9V	-3mV
Extended Data Fig. 8f	-10V	4mV
Extended Data Fig. 8h	6V	0mV